



POLITECNICO DI MILANO  
School of Industrial and Information Engineering

Master's Degree in Engineering Physics

# Femtosecond laser writing of integrated photonic circuits for multi-photon indistinguishability quantification

Candidate

**Riccardo Albiero**

mat. 919941

Supervisor

**Dr. Roberto Osellame**

Co-Supervisors

**Dr. Andrea Crespi**

**Dr. Giacomo Corrielli**



# Abstract

Multi-photon states play a crucial role in quantum metrology and in the photonic implementations of quantum computers. Therefore, the generation of many indistinguishable photons is one of the challenges of the current quantum technologies.

It is then required to develop tools and techniques for the characterization of the indistinguishability of multiple photons. In fact, while the photon-pair indistinguishability can be directly measured by means of the Hong-Ou-Mandel experiment, when higher number of photons are involved pairwise comparisons are not sufficient to assess the overall photons indistinguishability.

In this Thesis, we use an unpublished theoretical scheme to implement a reconfigurable integrated circuit which can be used to assess the genuine indistinguishability of four single photons. The circuit is fabricated by means of the femtosecond laser micromachining technology.

The device consists in a  $8 \times 8$  multiport interferometer, equipped with three integrated microheaters patterned on top, for the thermo-optical tuning of the internal phases. The design of the circuit fully exploits the unique potentialities of the fabrication technique, with the realization of 3D waveguide crossings. Optical waveguides and directional couplers have been optimized for the typical spectral range of quantum dot single photon sources (904 nm – 940 nm). These waveguides yield propagation losses as low as  $0.18 \text{ dB cm}^{-1}$ , and the circuit operation shows good independence from the polarization of impinging light.

To enhance the device portability, the integrated device was pigtailed with optical fiber arrays, achieving input-output losses lower than 2 dB.

This interferometer can be used for the verification and qualification of single photon sources, or as a tool for the empirical equalization of various degrees of freedom (e.g., temporal delays, polarization states) to obtain indistinguishable photons.



# Sommario

La generazione di diversi fotoni indistinguibili è una delle sfide delle attuali tecnologie quantistiche. Infatti gli stati multi-fotone hanno un ruolo rilevante in metrologia quantistica e per l'implementazioni di quantum computers basati sulla fotonica.

Risulta necessario, quindi, sviluppare delle tecniche per la caratterizzazione dell'indistinguibilità di  $n$ -fotoni. Tuttavia, se l'indistinguibilità di una coppia di fotoni può essere misurata direttamente mediante l'effetto Hong-Ou-Mandel, utilizzare dei confronti a coppie per la caratterizzare dell'indistinguibilità complessiva di uno stato multi-fotone non è sufficiente.

In questa tesi, utilizziamo uno schema teorico non ancora pubblicato per l'implementazione di un circuito integrato riconfigurabile per la stima dell'indistinguibilità di 4 fotoni. Il dispositivo è fabbricato mediante scrittura laser a femtosecondi.

Il dispositivo consiste in un interferometro multiporta  $8 \times 8$  e dotato di tre micro-riscaldatori utilizzati per la modulazione della fase interna dell'interferometro per mezzo dell'effetto termo-ottico.

La progettazione e la realizzazione del circuito sfruttano appieno le potenzialità uniche della tecnica di fabbricazione, realizzando strutture compatte e tridimensionali. Le guide d'onda e gli accoppiatori direzionali sono stati ottimizzati per la tipica gamma spettrale di emissione di sorgenti quantum dots, 904 nm–940 nm, mostrando perdite di propagazione di  $0.18 \text{ dB cm}^{-1}$  e una buona indipendenza dalla polarizzazione della luce in ingresso.

Per aumentare la portabilità e facilitare l'accoppiamento, è stata effettuata una connessione permanente con array di fibre, misurando perdite complessive di inserzione inferiori a 2 dB.

L'interferometro può essere utilizzato per caratterizzare di sorgenti di singoli fotoni, oppure come strumento per l'equalizzazione empirica dei vari gradi di libertà dei fotoni (es. ritardi temporali, polarizzazione) utilizzati in esperimenti di informazione quantistica.



# Introduction

Photon indistinguishability is a crucial concept in quantum optics. Since the first experimental observation of two-photon coalescence, known as Hong-Ou-Mandel effect, much effort has been devoted to study the quantum indistinguishability signatures for an increasing number of interfering particles.

Indeed, these phenomena are at the core of the computational complexity of linear optical networks, as exemplified by the boson sampling problem. Besides, quantification of multi-photon indistinguishability can be used for the characterization of the quality of single-photon sources, and developing new techniques for this task is a crucial step for the development of scalable quantum technology.

The realization of complex interferometric schemes, that may be needed also for assessing multi-photon indistinguishability, is effectively possible only with integrated optics. Indeed, integrated optical technologies offers great advantages in terms of stability, robustness and experimental footprint with respect to bulk approaches.

Among the many integrated-optics fabrication techniques, femtosecond laser micromachining has affirmed itself as an interesting technique for rapid prototyping of photonic quantum circuits. This technology allows the fabrication of high-quality waveguides in direct and cost-effective way, without the need of any lithographic step or clean-room facilities. In addition, this technology is intrinsically three-dimensional, allowing the exploration of circuit designs which would be otherwise impossible to realize with other fabrication techniques. Moreover, femtosecond laser-written photonic circuits being written in glass can be perfectly mode-matched to the optical fibres, which is a key requirement for the realization of low-loss processing nodes in quantum optical networks.

The aim of this Thesis work is the experimental realization of an integrated multi-port interferometer for the quantification of multi-photon indistinguishability, using an unpublished theoretical scheme devised by the researches of INF-CNR and of the Physics Department of Politecnico di Milano. In particular, the device allows direct measurements of the genuine 4-photons indistinguishability. The experiment is conducted together with a research group of the CNRS in Paris-Saclay, which will perform the quantum experiment using single-photon sources based on quantum dots. We will present the specifications and the design of the reconfigurable integrated circuit for the assessment of 4-photons indistinguishability. We will describe in detail the fabrication of the interferometer together with its optical characterization.

This Thesis is structured as follows. In Chapter 1 we recall some fundamental concepts on quantum optics and multi-photon indistinguishability, and introduce the

theoretical scheme for the interferometer. In Chapter 2 we review the femtosecond laser micromachining technique, for the fabrication of integrated optical circuits in transparent substrates. In Chapter 3 we introduce the experimental setup and the methods employed for the characterization of the device. In Chapter 4 we present the development and characterization of the basic optical components for the integrated device. In Chapter 5 we discuss on the design and characterization of the multiport interferometer. Finally, in Chapter 6, we discuss the fabrication and characterization of the microheaters for the reconfiguration of the internal phase terms. The fabrication and characterization processes have been carried out at the Physics Department of Politecnico di Milano.

# Contents

<b>Abstract</b>	<b>i</b>
<b>Sommario</b>	<b>iii</b>
<b>Introduction</b>	<b>v</b>
<b>1 Photon Indistinguishability and quantum interference</b>	<b>1</b>
1.1 Fundamentals of Second Quantization . . . . .	1
1.1.1 Quantization of electromagnetic field . . . . .	1
1.1.2 Photon . . . . .	2
1.2 Two-photon interference . . . . .	3
1.2.1 Particles distinguishability . . . . .	3
1.2.2 Hong-Ou-Mandel Experiment . . . . .	4
1.3 Need for multi-photon interference . . . . .	8
1.3.1 The boson sampling problem . . . . .	8
1.3.2 Quantum metrology . . . . .	9
1.4 Characterization of quantum indistinguishability . . . . .	10
1.4.1 Suppression laws . . . . .	10
1.4.2 Genuine multi-photon interference . . . . .	11
1.4.3 Photons indistinguishability bounds . . . . .	12
1.5 Proposed interferometer . . . . .	13
1.5.1 Circuit design . . . . .	13
1.5.2 Role of phase shifters . . . . .	14
1.5.3 Direct multi-photon interference . . . . .	15
<b>2 Femtosecond Laser Micromachining</b>	<b>19</b>
2.1 Femtosecond pulse interaction with dielectrics . . . . .	19
2.1.1 Plasma formation . . . . .	20
2.1.2 Relaxation and permanent modification . . . . .	21
2.2 Waveguide writing . . . . .	22
2.2.1 Focusing conditions . . . . .	22
2.2.2 Writing configuration . . . . .	23
2.2.3 Repetition rate and thermal effects . . . . .	24
2.2.4 Annealing process . . . . .	25
2.3 State of the art . . . . .	26
2.3.1 Passive integrated photonic circuits . . . . .	27

2.3.2	Reconfigurable integrated photonic circuits . . . . .	30
<b>3</b>	<b>Experimental Methods</b>	<b>35</b>
3.1	Waveguide writing setup . . . . .	35
3.1.1	General scheme . . . . .	35
3.1.2	Laser source . . . . .	35
3.1.3	Motion stages . . . . .	36
3.2	Chip post-processing . . . . .	37
3.2.1	Glass polishing . . . . .	37
3.2.2	Gold coating and resistor patterning . . . . .	37
3.2.3	Fiber pigtailling . . . . .	37
3.3	Characterization methods . . . . .	38
3.3.1	Microscope inspection . . . . .	38
3.3.2	Optical characterization setup . . . . .	39
3.3.3	Mode profiling . . . . .	40
3.3.4	Losses characterization . . . . .	40
<b>4</b>	<b>Optimization of waveguide components</b>	<b>43</b>
4.1	Waveguide optimization . . . . .	43
4.1.1	Optimization of propagation and coupling losses . . . . .	44
4.1.2	Characterization of bending losses . . . . .	46
4.2	Directional couplers optimization . . . . .	46
4.2.1	Coupled mode theory and best-fit . . . . .	47
4.2.2	Preliminary assessment of waveguide quality . . . . .	48
4.2.3	Coupling distance optimization . . . . .	49
4.2.4	Polarization sensitivity . . . . .	51
<b>5</b>	<b>Fabrication of passive interferometric circuit</b>	<b>53</b>
5.1	Circuit geometry design . . . . .	53
5.2	Device fabrication of the device . . . . .	57
5.2.1	Fabrication and preliminary characterization . . . . .	57
5.2.2	Insertion losses characterization at 925 nm . . . . .	57
5.2.3	Splitting ratio characterization at 925 nm . . . . .	58
<b>6</b>	<b>Fabrication of reconfigurable interferometric circuit</b>	<b>63</b>
6.1	Design of the thermal phase-shifters . . . . .	63
6.2	Characterization of the thermal phase-shifters . . . . .	66
6.3	Fiber pigtail and packaging . . . . .	68
	<b>Conclusions</b>	<b>71</b>
	<b>Ringraziamenti</b>	<b>73</b>
	<b>Bibliography</b>	<b>75</b>

# List of Figures

Figure 1.1	Scheme of the Hong-Ou-Mandel experiment and interference fringe.	4
Figure 1.2	Hong-Ou-Mandel experiment outcomes for fully distinguishable and fully indistinguishable particles. . . . .	5
Figure 1.3	Experimental result for three and two photon coincidence measures.	12
Figure 1.4	Scheme for the interferometer for bound the genuine four-photon indistinguishability. . . . .	13
Figure 1.5	General scheme of the $N$ -mode interferometer. . . . .	14
Figure 1.6	Procedure for the reduction of the number of phase shifters in the device. . . . .	15
Figure 1.7	Scheme of the $N$ -mode interferometer equivalent to the one in Figure 1.5. . . . .	16
Figure 2.1	Nonlinear absorption processes . . . . .	20
Figure 2.2	Permanent modifications for different pulse energies. . . . .	22
Figure 2.3	Waveguide writing configurations: longitudinal and transversal.	23
Figure 2.4	Thermal effects in the focal volume. . . . .	24
Figure 2.5	Thermal annealing: temperature profile and effects on the waveguide cross section. . . . .	26
Figure 2.6	Scheme of a directional coupler. . . . .	27
Figure 2.7	Scheme of a symmetric polarization-insensitive directional coupler.	28
Figure 2.8	Scheme of the circuits for generation and verification of 8-mode multipartite entanglement. . . . .	29
Figure 2.9	Scheme of 5-mode interferometer for boson sampling experiments.	30
Figure 2.10	Scheme of 3D network of directional couplers. . . . .	31
Figure 2.11	Scheme of the reconfigurable Mach-Zender interferometer. . . .	31
Figure 2.12	Scheme of a reconfigurable chip for multiphase estimation. . . .	32
Figure 2.13	Thermal stability of thermal shifters. . . . .	33
Figure 3.1	Waveguide writing setup. . . . .	36
Figure 3.2	Fiber array input facet. . . . .	38
Figure 3.3	End-fire coupling configuration. . . . .	39
Figure 4.1	Losses figures at different values of laser irradiation power. . . .	45
Figure 4.2	Bending losses for S-bends with different curvature radii. . . . .	46
Figure 4.3	Reflectivity values of directional couplers as a function of the coupling length. . . . .	49

Figure 4.4	Reflectivity values of directional couplers as a function of the coupling distance. . . . .	50
Figure 4.5	Reflectivity values of directional couplers measured with H- and V-polarized light. . . . .	51
Figure 5.1	Theoretical scheme and integrated optical design of the 8-mode interferometer. . . . .	54
Figure 5.2	Different three dimensional layout for the 8-mode interferometer.	55
Figure 5.3	Single-mode insertion losses for H- and V-polarized light. . . . .	59
Figure 5.4	Scheme of a two rows cascading directional couplers. . . . .	59
Figure 5.5	Scheme of a directional coupler with a differential loss between the output modes. . . . .	60
Figure 6.1	Top-view of the interferometer with three thermal phase-shifters.	65
Figure 6.2	Scheme of the electrical connections and ablation pattern for the thermal shifters. . . . .	65
Figure 6.3	Scheme of the Young interference experiment. . . . .	67
Figure 6.4	Power-phase coefficient retrieval procedure. . . . .	69
Figure 6.5	Final device. . . . .	70

# List of Tables

Table 4.1	Optimal inscription parameters for single-mode waveguides. .	44
Table 5.1	Geometrical parameters of the multiport integrated interferometers. . . . .	57
Table 5.2	Reflectivity values for multiport interferometers varying the coupling distances of the directional couplers. . . . .	58
Table 5.3	Reflectivity values of the directional couplers with coupling distance $d_c = 6.8 \mu\text{m}$ . . . . .	61
Table 5.4	Reflectivity values of the directional couplers with coupling distance $d_c = 6.9 \mu\text{m}$ . . . . .	61
Table 6.1	Thermal shifters resistance measured with a driving voltage of 100 mV. . . . .	66



# Chapter 1

## Photon Indistinguishability and quantum interference

In this Chapter photon indistinguishability is briefly presented. First, we introduce the concept of photon and the formalism of the second quantization with the creation and annihilation operators. Then we present the properties of indistinguishable photons and the Hong-Ou-Mandel experiment. We also discuss few applications of the multi-photon interference and in some ways to characterize the indistinguishability of a set of  $n$  photons are discussed. Finally, we introduce the proposed interferometer for measuring multi-photon indistinguishability.

### 1.1 Fundamentals of Second Quantization

A quantum theory of radiation is indispensable to understand the properties of light. The field quantization is developed following a formal analogy with the quantum mechanics of the harmonic oscillator. The electromagnetic field is described with an *infinite* product of such generalized harmonic oscillators.

The aim of this Section is to introduce the quantized electromagnetic field and use this concept for introducing the notion of photon and of Fock states.

#### 1.1.1 Quantization of electromagnetic field

The derivation for the electric field  $\mathbf{E}(\mathbf{r}, t)$  as function of the position  $\mathbf{r}$  and the time  $t$  is reported here, the formulation of the magnetic field  $\mathbf{B}(\mathbf{r}, t)$  is analogous. The electromagnetic field can be written in terms of the Fourier components of the normal modes of a cavity of volume  $V$  [1]:

$$\begin{aligned}\mathbf{E}(\mathbf{r}, t) &= \mathbf{E}^+(\mathbf{r}, t) + \mathbf{E}^-(\mathbf{r}, t) \\ &= \sum_k \sqrt{\frac{\hbar\omega_k}{2\epsilon_0 V}} \mathbf{e}_k [\alpha_k e^{-i\omega_k t + i\mathbf{k}\cdot\mathbf{r}} + \text{c.c.}] \end{aligned} \quad (1.1)$$

where the summation runs over all modes  $k$  with frequency  $\omega_k$ ,  $\alpha_k$  is the amplitude

of the oscillation,  $\mathbf{e}_k$  represent the polarization vector of the field while  $\hbar$  is the Planck constant and  $\varepsilon_0$  is the vacuum permittivity.

The classical Hamiltonian of the electromagnetic field is the following [1]:

$$\mathcal{H} = \frac{1}{2} \int dV \left[ \varepsilon_0 \mathbf{E}^2(\mathbf{r}, t) + \frac{1}{\mu_0} \mathbf{B}^2(\mathbf{r}, t) \right] \quad (1.2)$$

where  $\mu_0$  is the magnetic permeability of vacuum and the integral is taken over the whole volume  $V$  of the cavity. The second quantization procedure consists in turning each amplitude of (1.1) into an operator. We consider the oscillator amplitudes  $\alpha_k$  and  $\alpha_k^*$ , corresponding to harmonic motion, to be quantized by replacing  $\alpha_k \rightarrow \hat{a}_k$  and  $\alpha_k^* \rightarrow \hat{a}_k^\dagger$ .

Substituting the expressions of  $\mathbf{E}(\mathbf{r}, t)$  and  $\mathbf{B}(\mathbf{r}, t)$  written in terms of quantized Fourier components in (1.2) and integrating<sup>1</sup> over the whole volume  $V$  the Hamiltonian of the system can be written as:

$$\mathcal{H} = \frac{1}{2} \sum_k \hbar \omega_k (\hat{a}_k^\dagger \hat{a}_k + \hat{a}_k \hat{a}_k^\dagger) \quad (1.3)$$

The operators  $\hat{a}_k^\dagger$  and  $\hat{a}_k$  are, respectively, the creation and annihilation operators. They satisfy the bosonic commutation relation  $[\hat{a}_k^\dagger, \hat{a}_k^\dagger] = 0$  and are equivalent to the ladder operators for the harmonic oscillators, putting or extracting quanta of energy from the electromagnetic field.

### 1.1.2 Photon

Wave-particle duality is a emergent paradigma in quantum mechanics. In the second quantization picture, the photon is a discrete excitation of a mode  $k$  of the electromagnetic field in a cavity.

Using the commutation relations for the creation and annihilation operators associated to photons the Hamiltonian (1.3) can be recast as

$$\begin{aligned} \mathcal{H} &= \sum_k \hbar \omega_k \left( \hat{a}_k^\dagger \hat{a}_k + \frac{1}{2} \right) \\ &= \sum_k \hbar \omega_k \left( \hat{n}_k + \frac{1}{2} \right) \end{aligned} \quad (1.4)$$

where the number operator  $\hat{n}_k = \hat{a}_k^\dagger \hat{a}_k$  has been introduced, which describes the average number of photons in a given mode  $k$ .

Eigenstates of the number operator are the Fock states, quantum states in which the number of particles is a fixed integer:

$$\hat{a}^\dagger \hat{a} |n\rangle = n |n\rangle. \quad (1.5)$$

The operators  $\hat{a}$  and  $\hat{a}^\dagger$  are raising and lowering operators on a series of equally spaced

---

<sup>1</sup>Where mixed terms are simplified using the formula:  $\int e^{\pm i(\mathbf{k}-\mathbf{k}')\cdot\mathbf{r}} dV = V \delta_{\mathbf{k},\mathbf{k}'}$

eigenstates:

$$\hat{a}^\dagger |n\rangle = \sqrt{n+1} |n+1\rangle \quad (1.6)$$

$$\hat{a} |n\rangle = \sqrt{n} |n-1\rangle \quad (1.7)$$

$$\hat{a} |0\rangle = |0\rangle \quad (1.8)$$

The expressions (1.6) explicit the action of the creation and annihilation operators. The application of  $\hat{a}$  removes a photon from the system producing a state with one less quantum of energy. Alternatively, the application of  $\hat{a}^\dagger$ , adds a photon to the system resulting in a state with an additional quantum of energy.

They can be used to generate all possible Fock states starting from the ground state  $|0\rangle$  by a successive applications of the creation operator:

$$|n\rangle = \frac{(\hat{a}^\dagger)^n}{\sqrt{n!}} |0\rangle. \quad (1.9)$$

## 1.2 Two-photon interference

### 1.2.1 Particles distinguishability

In classical mechanics all particles are distinguishable. They can be labelled and all the properties of the particles can be investigated, in principle, with an infinite degree of precision.

In quantum mechanics the picture is completely different. A particle is described by a wavefunction and therefore its observables have a precise value only immediately after a measurement process [2]. In-between measurements the particle's observables do not possess definite values. As time passes, the wavefunctions of a multi-particle system spread and overlap making it impossible to follow the trajectories of individual particles and, therefore, to distinguish them.

A notion of particle indistinguishability can be introduced, based on the physical observables of the system [3]:

*Two states that differ only by a permutation of identical particles are physically equivalent*

This means that any *observable* of the system does not change after a mere permutation or swap of particles.

This condition imposes a symmetry constraint to the wavefunction that can be either fully symmetric or fully antisymmetric. In a second quantization formalism the symmetrization of the wavefunction is guaranteed by the commutation relations of the creation and annihilation operators. In the case of photons (or bosons in general) the wavefunction has to be completely symmetric and the operators  $\hat{a}$  and  $\hat{a}^\dagger$  must satisfy:

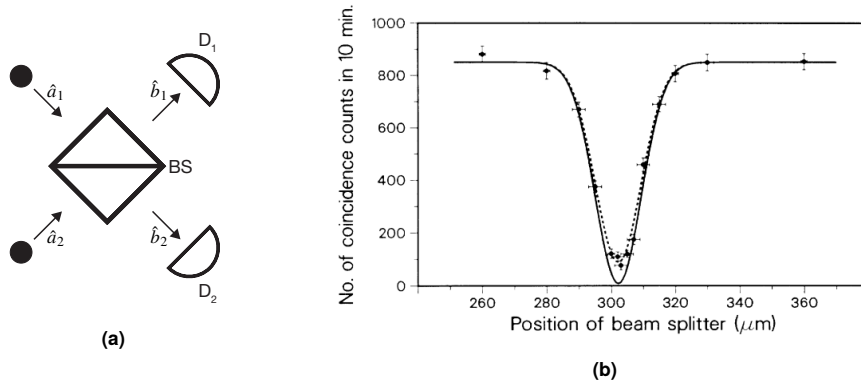


**Figure 1.1:** **a)** Basic scheme of a Hong-Ou-Mandel experiment. Two photons are injected in the different input channels of a beam-splitter and, at the output, the coincidence events are recorded. **b)** Typical interference fringe measured as a function of the relative delay between photons. [4].

$$[\hat{a}_\phi, \hat{a}_\lambda] = 0 \tag{1.10}$$

$$[\hat{a}_\phi^\dagger, \hat{a}_\lambda^\dagger] = 0 \tag{1.11}$$

$$[\hat{a}_\phi^\dagger, \hat{a}_\lambda] = \langle \phi | \lambda \rangle \tag{1.12}$$

where the subscripts  $\phi$  and  $\lambda$  indicate two different particles.

### 1.2.2 Hong-Ou-Mandel Experiment

The Hong-Ou-Mandel (HOM) effect [4] is a simple yet powerful manifestation of quantum interference of the bosonic field associated to photons.

It occurs in the simple experiment which consists in sending two photons to the different input channels of a balanced beam-splitter and in measuring the coincidence events at the output, in which each photon exits in a different channel. The basic scheme is reported in Figure 1.1a.

#### Distinguishable particles

We consider the case of a pair of fully distinguishable particles (Figure 1.2a). Photons propagate independently and each of them can be either transmitted or reflected. At the output of the beam-splitter we can observe both states with multiple particles in the same output mode (bunched states) and states with a single particle per mode (anti-bunched states) [5].

We can write:

$$\mathcal{P}(1, 1) = p_{1,1}p_{2,2} + p_{1,2}p_{2,1} \tag{1.13}$$

$$\mathcal{P}(0, 2) = p_{1,2}p_{2,2} \tag{1.14}$$

$$\mathcal{P}(2, 0) = p_{1,1}p_{2,1} \tag{1.15}$$

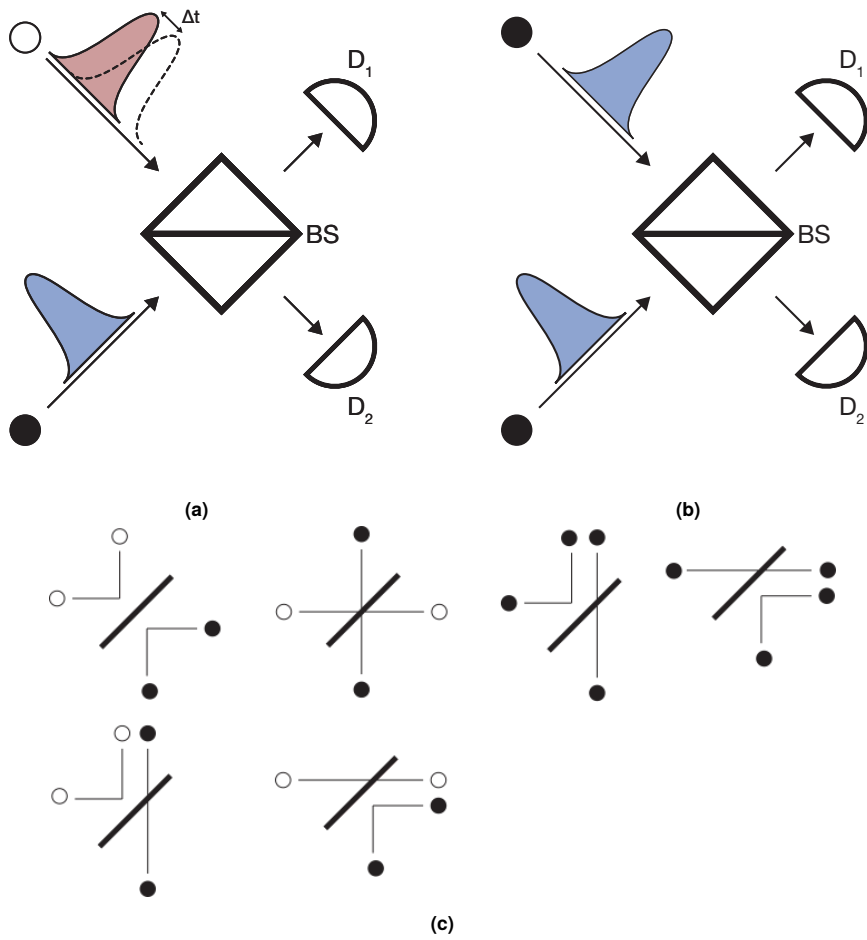


**Figure 1.2:** Schematic view of HOM experiments using photon pairs with different distinguishability. In panel **a**) is depicted the case of distinguishable photons while in panel **b**) is reported the case of indistinguishable photons. In **c**) is depicted a representation of the possible output events of the HOM experiment in the case of fully distinguishable photons (left) and fully indistinguishable photons (right). In the latter case not all classical permitted output are possible, only bunching state are observed.

where  $p_{i,j}$  are the classical probability of having the particle in channel  $i$  to be scattered to channel  $j$ . Since we are considering a balanced beam-splitter, all  $p_{i,j}$  events are equiprobable (Figure 1.2, left panel) and we obtain simply:

$$\mathcal{P}(1, 1) = \frac{1}{2} \quad (1.16)$$

$$\mathcal{P}(0, 2) = \mathcal{P}(2, 0) = \frac{1}{4} \quad (1.17)$$

### Indistinguishable particles

In the case of indistinguishable particles a treatment with second quantization formalism is needed. We consider the input state as:

$$|\psi\rangle_{in} = \hat{a}_1^\dagger \hat{a}_2^\dagger |0\rangle \quad (1.18)$$

where  $\hat{a}_1^\dagger$  and  $\hat{a}_2^\dagger$  are the bosonic creation operators in the two beam-splitter input modes.

The output state can be computed from the input state using the balanced beam-splitter unitary matrix  $U_{BS}$  [6]:

$$\begin{bmatrix} \hat{b}_1^\dagger \\ \hat{b}_2^\dagger \end{bmatrix} = U_{BS} \cdot \begin{bmatrix} \hat{a}_1^\dagger \\ \hat{a}_2^\dagger \end{bmatrix} = \frac{1}{\sqrt{2}} \begin{bmatrix} 1 & i \\ i & 1 \end{bmatrix} \cdot \begin{bmatrix} \hat{a}_1^\dagger \\ \hat{a}_2^\dagger \end{bmatrix} \quad (1.19)$$

obtaining:

$$\begin{aligned} |\psi\rangle_{out} &= U_{BS} |\psi\rangle_{in} \\ &= \hat{b}_1^\dagger \hat{b}_2^\dagger |0_1, 0_2\rangle \\ &= \frac{1}{\sqrt{2}} \left[ i \left( \hat{a}_1^\dagger \hat{a}_1^\dagger - \hat{a}_2^\dagger \hat{a}_2^\dagger \right) + \hat{a}_2^\dagger \hat{a}_1^\dagger - \hat{a}_1^\dagger \hat{a}_2^\dagger \right] |0\rangle \end{aligned} \quad (1.20)$$

By applying the boson commutation relations (1.10) we notice that  $\hat{a}_1^\dagger \hat{a}_2^\dagger = \hat{a}_2^\dagger \hat{a}_1^\dagger$  and thus the last two terms interfere destructively. The final output will be:

$$|\psi_{out}\rangle = \frac{i}{\sqrt{2}} (|2, 0\rangle - |0, 2\rangle) \quad (1.21)$$

where we have the coherent superposition of both particles in either mode 1 or mode 2 and:

$$\mathcal{P}(|0, 2\rangle) = \mathcal{P}(|2, 0\rangle) = \frac{1}{2} \quad (1.22)$$

$$\mathcal{P}(|1, 1\rangle) = 0 \quad (1.23)$$

This means that only the bunched outcomes are possible, while the anti-bunched state is strictly suppressed by quantum interference effect (Figure 1.2c, right panel).

### Partially distinguishable particles

In the case of photons with partial indistinguishability, a generic two-photon state  $|\psi\rangle_{in}$  can be written as:

$$|\psi\rangle_{in} = \hat{a}_A^\dagger \hat{a}_B^\dagger |0\rangle \quad (1.24)$$

where each particle carries a degree of freedom (e.g. arrival time, polarization, spectrum, etc.),  $|A\rangle$  and  $|B\rangle$  respectively, that allows to distinguish them, while all the other degrees of freedom are assumed to be identical. The subscript  $A$  ( $B$ ) indicates that the creation operator creates a photon in  $|A\rangle$  ( $|B\rangle$ ).

The description of one of the partially distinguishable degrees of freedom can be recast as a linear combination of a completely indistinguishable and a completely distinguishable contribution [5]. For  $|B\rangle$  we can write:

$$|B\rangle = \underbrace{\langle A|B\rangle}_{c^\parallel} |A\rangle + \underbrace{\left(\sqrt{1 - \langle A|B\rangle^2}\right)}_{c^\perp} |\bar{B}\rangle. \quad (1.25)$$

where  $|\bar{B}\rangle$  is a state orthogonal to  $|A\rangle$ . It follows:

$$|\psi\rangle_{in} = \left( c^\parallel \hat{a}_A^\dagger \hat{a}_B^\dagger + c^\perp \hat{a}_A^\dagger \hat{a}_{\bar{B}}^\dagger \right) |0\rangle \quad (1.26)$$

where  $c^\parallel$  and  $c^\perp$  are probabilities for the photons to be intrinsically indistinguishable or distinguishable.  $c^\parallel$  can be considered as a measure of the intrinsic indistinguishability.

From an experimental point of view, identical particles can become partially distinguishable by tweaking a particular degree of freedom such as polarization or arrival time. With this control over the particles state, the transition between fully distinguishable and fully indistinguishable particles can be explored. In the original HOM experiment the arrival time between photons was chosen to tune the photon indistinguishability. We can consider two partially distinguishable wave packets, in temporal modes that are described by  $|t_1\rangle$  and  $|t_2\rangle$ , respectively.

In analogy with the previous derivation, the temporal mode  $|t_2\rangle$  can be written as a linear combination of a contribution parallel to  $|t_1\rangle$  and a contribution  $|\bar{t}_2\rangle$  which is orthogonal to  $|t_1\rangle$ :

$$|t_2\rangle = c^\parallel |t_1\rangle + c^\perp |\bar{t}_2\rangle. \quad (1.27)$$

In this way, the first term gives rise to quantum interference while the second term behaves as a fully distinguishable classical particle. Repeating the calculations of (1.20) we would not retrieve a perfect cancellation of the coincidence state  $|1, 1\rangle$  and the probability of detecting such state reads:

$$\mathcal{P}(1, 1) = \frac{1}{2} \left( 1 - |c^\parallel|^2 \right) \quad (1.28)$$

By continuously changing the arrival time difference  $\Delta t$  between the two temporal modes of the photons one obtains an interference fringe like the one reported in Figure 1.1b.

### 1.3 Need for multi-photon interference

The Hong-Ou-Mandel effect is a striking manifestation of the quantum properties of light, showing the bunching tendency of bosons, and it constitutes a pivotal result in quantum optics.

A natural step, at this point, would be to generalize the experiment to a generic  $n$ -photon case, and investigate multi-photon interference. Multi-photon interference and multi-photon indistinguishability are key elements to develop advanced quantum photonics applications[7, 8, 9, 10, 11, 12]. We briefly review in the following two of them.

#### 1.3.1 The boson sampling problem

The boson sampling problem consists in sampling from the output distribution of  $n$  indistinguishable photons that interfere through a linear  $m$ -mode interferometer described by a Haar-random unitary matrix with  $m \gg n$ .

We can present the problem by considering a set of  $m$  modes with associated bosonic creation operator  $\hat{a}_i^\dagger$ . The generic Fock state of  $n$  photons is:

$$|\psi_{in}\rangle = |s_1, s_2, \dots, s_m\rangle = \prod_{i=1}^m \frac{1}{\sqrt{s_i!}} (\hat{a}_i^\dagger)^{s_i} |0\rangle \quad (1.29)$$

where  $s_i$  are non-negative integers that count the number of photons in each mode and  $\sum s_i = n$ . The  $m$ -modes interferometer is described by a unitary transformation  $U$  whose action determines the evolution of the creation operators  $\hat{a}_i^\dagger \rightarrow \sum_{j=1}^m U_{ij} \hat{a}_j^\dagger$ .

The transition probability between an input state  $|S\rangle = |s_1, s_2, \dots, s_m\rangle$  and an output state  $|T\rangle = |t_1, t_2, \dots, t_m\rangle$  can be written as [13]:

$$\mathcal{P}(|S\rangle \rightarrow |T\rangle) = \frac{|\text{Per}(U_{S,T})|^2}{\prod_{i=1}^m s_i! t_i!} \quad (1.30)$$

where  $U_{S,T}$  is a  $n \times n$  sub-matrix of  $U$  constructed by taking  $t_i$  copies of the  $i$ -th row of  $U$  and  $s_j$  copies of the  $j$ -th column.  $\text{Per}(A)$  is the permanent operator defined as:

$$\text{Per}(A) = \sum_{\sigma \in P_n} \prod_{i=1}^n a_{i, \sigma(i)} \quad (1.31)$$

where  $A = (a_{ij})_{i,j \in [n]}$  and the summation runs over all the permutations,  $P_n$ , of  $\{1, \dots, n\}$ .

For matrices  $U$  without particular symmetries, the permanent is hard to compute. In terms of complexity, it is a #P-hard problem since the best classical algorithms have a computational time that exponentially with  $n$ .

In their seminal work [14], Aaronson and Arkhipov shifted the attention to a sampling problem where the computational task consists in producing a sample from some probability distribution sufficiently close to the ideal one.

Arguments from Ref. [14] provide strong evidences against the possibility of an efficient classical simulation of boson sampling, while this problem can be tackled by a *dedicated* quantum hardware. In this sense, the boson sampling problem is a candidate to obtain a quantum advantage, i.e. an experimental demonstration of a quantum device capable of performing a computational task unambiguously faster than present day classical computers.

It is important, then, to scale the number of photons up to the point of a provable quantum advantage with respect to the current classical computers. In this scenario, multi-photon indistinguishability is important since an overall distinguishability between the photons degrades the hardness of the classical simulation and thus a strong effort should be dedicated to building sources characterized by a high level of photon indistinguishability.

Since the original proposal of Aaronson and Arkhipov, several theoretical studies have focused on different aspects of the problem, including the role of experimental imperfections in the complexity of classical simulation, as well as proposals of new variants of the original problem. The first experimental instances of the boson sampling were reported in Ref. [15, 16, 17, 8]. Finally, in 2020 quantum advantage using photonic boson sampling has been proved [18].

### 1.3.2 Quantum metrology

Optical measurements conducted with classical states of light (coherent light) are limited in precision by the granularity of photons. In particular, in coherent light states photons follows a Poissonian statistics and the number of detected photons,  $N$ , has a standard deviation  $\Delta N = \sqrt{\langle N \rangle}$ , where  $\langle N \rangle$  denotes the mean number of photons detected.

This determines that the measured quantity will have a signal-to-noise ratio (SNR):

$$\text{SNR} \propto \frac{\Delta N}{\langle N \rangle} = \frac{1}{\sqrt{\langle N \rangle}} \quad (1.32)$$

which is referred to as the shot-noise limit.

An interesting problem in quantum metrology is to perform measurements that are able to beat the shot-noise limit. Employing non-classical states of lights, characterized by a sub-Poissonian statistics ( $\Delta N < \sqrt{\langle N \rangle}$ ), offer precision enhancement in interferometric scenarios by reducing the photon number fluctuations. This leads toward measurements with  $1/\langle N \rangle$  precision scaling, which is the so-called the Heisenberg limit [19].

For instance, one could perform interferometry with NOON states which are path entangled states of  $N$  photons across two modes:

$$|\text{NOON}\rangle = \frac{1}{\sqrt{2}} (|N\rangle |0\rangle + |0\rangle |N\rangle). \quad (1.33)$$

These states offer both super-resolution ( $N$ -fold decrease in fringe period) and super-sensitivity (enhanced precision  $\Delta\Phi \propto 1/\langle N \rangle$ ), and they are the optimal state for low-flux sensing in the lossless regime [20, 21].

Of course, these protocols are based on multi-photon interference which, in turn, is based on multi-photon indistinguishability.

## 1.4 Characterization of quantum indistinguishability

In the following, the discussion of Section 1.2 is generalized to the  $n$ -photon case. We discuss the differences between two-photon and multi-photon interference and report a method to characterize the multi-photon indistinguishability.

### 1.4.1 Suppression laws

The bosonic nature of photons determines the symmetry of the wavefunction describing the multi-particle system which, in turns, translates into a bunching tendency.

The bunching tendency is enhanced when photons evolution is characterized by specific symmetry, for example, the evolution through symmetrical multiport beam-splitters. Various studies and experimental works [13, 22, 23, 24, 25, 26], shows enhancement of bunched states and suppression of anti-bunched events, when  $n$  photons interfere in multiport circuits. The balanced beam-splitter of the HOM effect is the simplest example of such symmetric optical circuit and the suppression of the anti-bunched state  $|1, 1\rangle$  has been computed explicitly in Section 1.2.

We can consider, for the general  $n$ -photon case, an arrangement of  $n$  particles propagating through a  $n$ -modes Fourier multiport described by an unitary matrix  $U$  whose terms are defined as [13]:

$$U_{jk} = \frac{1}{\sqrt{n}} e^{i\frac{2\pi}{n}(j-1)(k-1)}. \quad (1.34)$$

The initial and final state can be described by a vector  $|s\rangle = |s_1, s_2, \dots, s_n\rangle$  and  $|t\rangle = |t_1, t_2, \dots, t_n\rangle$  where  $s_i$  and  $t_i$  indicates the number of particle in the  $i$ -th mode and  $\sum s_i = \sum t_i = n$ .

In the case of *distinguishable* particle, when computing the output state probability of a certain arrangement, classic combinatorics applies:

$$\mathcal{P}_{class}(\mathbf{t}) = \frac{1}{n^n} \frac{n!}{\prod_{j=1}^n t_j!}. \quad (1.35)$$

We can notice that anti-bunched events,  $|t\rangle = |1, 1, \dots, 1\rangle$ , are realized with a probability  $n!/n^n$ . On the other hand, bunching events,  $|t\rangle = |0, 0, \dots, n, \dots, 0\rangle$ , are realized with a probability  $1/n^n$  suffering a decrease by a factor of  $n!$ .

In case of fully *indistinguishable* quantum particles, the situation is analogous to the boson sampling problem introduced in Section 1.3. By adapting equation (1.30) to

the problem under consideration, one finds

$$\mathcal{P}_{qm}(\mathbf{t}) = \frac{|\text{Per}(U_{s,t})|^2}{\prod_j s_j! t_j!} \quad (1.36)$$

Following Ref. [13], we notice that the bunched state  $|t\rangle = |n, 0, \dots, 0\rangle$  is enhanced by a factor  $n!$  with respect to the classical case. In the case of a multiport circuit with a specific symmetry, simple suppression rules for the generic arrangement  $|t\rangle$  at the output, by exploiting the regularity of  $U$ , have been demonstrated for Fourier and Sylvester interferometers [13, 22].

Suppression rules summarize in a simple analytical form the existence of collective effects of quantum interference that overshadow the statistical (*classical*) effects on the output state configuration. A simple suppression law for Fourier multiports, and input states with cyclic symmetry, is due to Tichy *et al.* [13]. Output states  $|t\rangle$  are completely suppressed if:

$$\text{mod} \left( \sum_{i=1}^n d_i(t), n \right) \neq 0 \quad (1.37)$$

where  $d_j(t)$  are the components of the mode assignment list  $\mathbf{d}(t)$  whose  $i$ -th entry is the exit mode of the  $i$ -th particle.

As one would expect, a general bunching tendency of the photons is recovered also in the  $n$ -photon case for which output arrangements with high number of particles in a single mode are preferred.

### 1.4.2 Genuine multi-photon interference

The simple two-photon interference of the HOM experiment allows to gauge the indistinguishability of the impinging photons, which is indeed estimated by the visibility of the interference dip. However, a generalization of the HOM experiment for the case of  $n$  photons is not straightforward. By scaling the experiment to a number of photons higher than two, we find a much richer scenario with respect to the two-photon case [27, 28].

In particular, in the interference process, collective quantities are involved which are characteristic of the whole set of photons rather than the individual photon pairs.

The simplest example of such collective quantities is reported in Ref. [28] where the case  $n = 3$  was considered. The probability of  $|1, 1, 1\rangle$  output state is studied when a single photon is injected in each mode of a balanced three-mode beam-splitter (tritter).

This probability,  $\mathcal{P}_{111}$ , reads:

$$\mathcal{P}_{111} = \frac{1}{9} [2 + 4r_{12}r_{23}r_{31} \cos(\varphi) - r_{12}^2 - r_{23}^2 - r_{31}^2] \quad (1.38)$$

where  $\varphi$  is the collective *triad phase* defined as  $\varphi = \varphi_{12} + \varphi_{23} + \varphi_{31}$  and both  $r_{ij}$  and  $\varphi_{ij}$  came from the photon-pair inner products  $\langle \psi_i | \psi_j \rangle = r_{ij} e^{i\varphi_{ij}}$ . As in the HOM experiment,  $r_{ij}$  can be interpreted as a measure of distinguishability of a pair of photons.

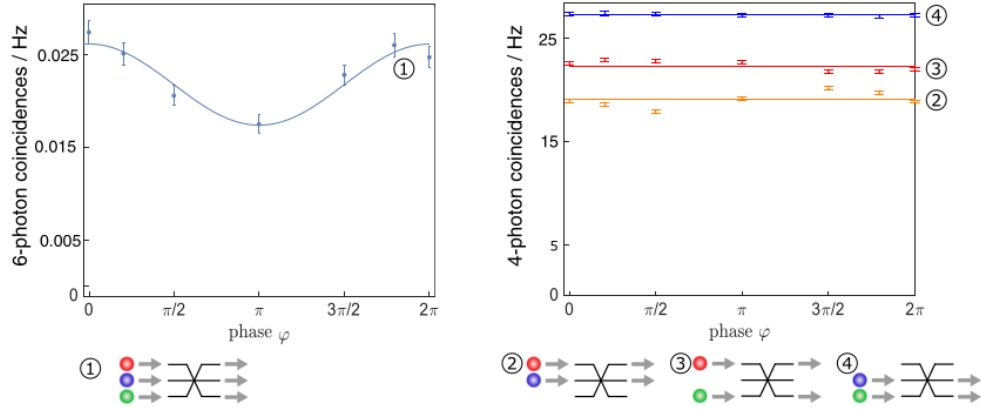


**Figure 1.3:** Experimental result for three and two photon coincidence measures. In the left panel is shown the variation of  $\mathcal{P}_{111}$  as a function of the triad phase  $\varphi$ . In the right panel the are shown coincidence measures with different photon-pairs as the triad phase  $\varphi$  varies. [28]

From equation (1.38) is evident that the probability of the three-photon anti-bunched state depend on the collective phase  $\varphi$ . By changing this phase term an interference dip is visible, while HOM experiments with photon pairs remain unaltered as shown in Figure 1.3. It is clear that the multi-photon interference extends beyond the pairwise distinguishability of photons which is not sufficient to describe the complete photons' behaviour in a scattering process.

### 1.4.3 Photons indistinguishability bounds

Ref. [29, 26] give a method for estimating multi-photon indistinguishability for a set of  $n$  photons using a series of cross-pairs HOM tests. In those works, the theory is developed by explicitly for the case of  $n = 4$ , but the formalism introduced can be generalized to a generic  $n$ .

We consider the linear interferometer represented in Figure 1.4 with six modes. Photons are injected in inputs  $A, B, C$  and  $D$  and multiple HOM tests are performed at the output. The overlaps  $r_{ij}$  between the photon states  $i$  and  $j$  can be estimated experimentally via the bunching probability  $\mathcal{P}_{ij}$  in a HOM experiment between photons  $i$  and  $j$ :

$$\mathcal{P}_{ij} = \frac{1 + |r_{ij}|^2}{2} \quad (1.39)$$

The four-photon state can be describe in terms of its density matrix using a model that is analogous to (1.26):

$$\rho = c^{\parallel} \rho^{\parallel} + \sum_{s>1} c^{\perp} \rho_s^{\perp}, \quad (1.40)$$

where  $\rho^{\parallel}$  is a pure state of four perfectly indistinguishable photons and  $\rho_s^{\perp}$  are pure states where at least two photons are orthogonal. In this way we identify the degree of *genuine* indistinguishability with  $c^{\parallel}$ , as it represent the probability of preparing

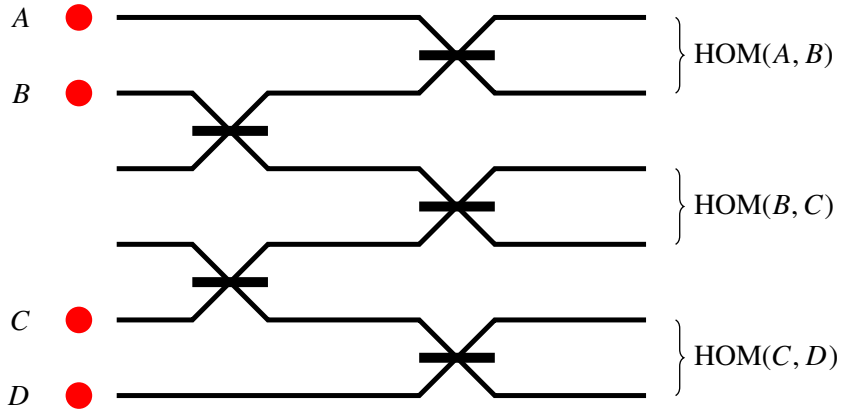


**Figure 1.4:** Scheme for four-photon experiment. The circuit is a 6-mode interferometer with balanced beam-splitters (50:50). The red dots represent the photons injected in the interferometer and at the output multiple HOM tests can be performed.

perfectly indistinguishable photons.

A single HOM experiment is not enough for a complete characterization of the  $c^{\parallel}$  term in the multi-photon case. However, with this circuit we are able to perform various HOM experiments between different pairs of photons. Combining all this information allows us to give non-trivial upper and lower bounds to the *genuine* indistinguishability term  $c^{\parallel}$ :

$$r_{AB} + r_{BC} + r_{CD} - 2 \leq c^{\parallel} \leq \min(r_{AB}, r_{BC}, r_{CD}) \quad (1.41)$$

This derivation shows how the use of multiple HOM test can give non-trivial bounds to the genuine indistinguishability term; however the precise value of  $c^{\parallel}$  is not estimated.

## 1.5 Proposed interferometer

In the following section we present the scheme of a  $N$  mode interferometer, for characterizing the genuine  $n$ -photon indistinguishability. The circuit solves the aspects highlighted in the previous sections as it allows to have a direct, HOM-like characterization of the genuine  $n$ -photon indistinguishability. This scheme has been devised by researches of INF-CNR and of the Physics Department of Politecnico di Milano, and it has not been published yet. An integrated optical version of the circuit will be realized in the experimental part of this Thesis work.

### 1.5.1 Circuit design

The circuit is a  $N = 2n$  modes interferometer, composed by two rows of cascaded balanced beam-splitters connected in the fashion of Figure 1.5.

Beam-splitters of the first row connect each odd mode to the adjacent even mode and, analogously, the beam-splitters of the second row connect each odd mode to the adjacent even mode. In the second row, the  $N$ -th mode is connected to the first one in

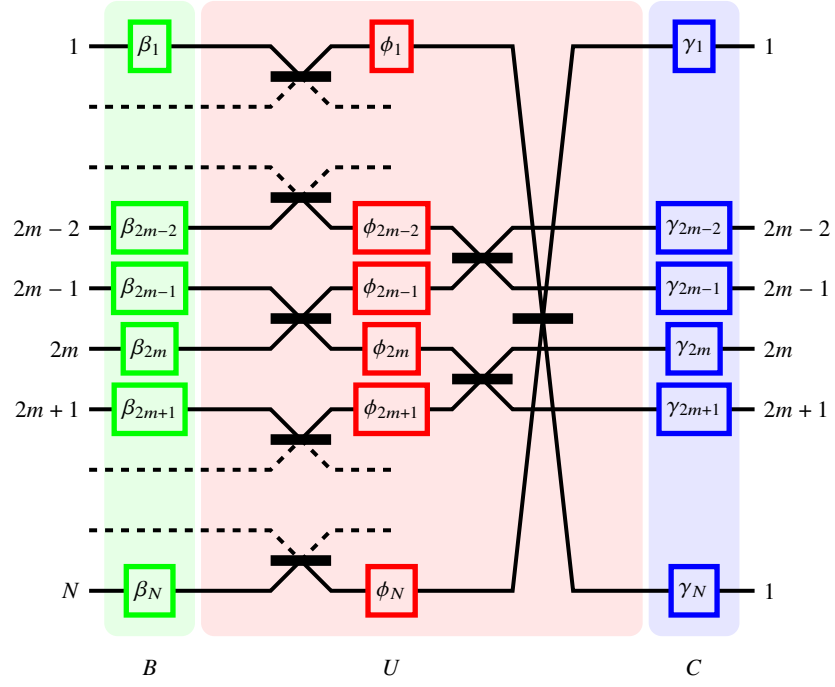


**Figure 1.5:** Scheme of the  $N$ -mode interferometer where all the phase terms are highlighted. In  $\beta_i$  are the input phase terms,  $\gamma_i$  are the output phase terms, while  $\phi_i$  are the phases of the waveguides of the interferometer's optical modes.

order to achieve a perfect circular symmetry. Phase shifters are placed in the inputs, outputs and between the two rows of beam-splitters, in order to model arbitrary phase delays in the optical modes.

### 1.5.2 Role of phase shifters

First of all, we can easily show that the phase terms at the input (before the first row of beam-splitters) and at the output (after the second row of beam-splitters) do not influence the output distribution for any Fock state at the input. Indeed, these terms can be factored out of the matrix of the actual interferometer and represented with diagonal matrices,  $B$  and  $C$ , respectively (see Figure 1.5):

$$B = \begin{bmatrix} e^{i\beta_1} & & \\ & \ddots & \\ & & e^{i\beta_N} \end{bmatrix} \quad C = \begin{bmatrix} e^{i\gamma} & & \\ & \ddots & \\ & & e^{i\gamma_N} \end{bmatrix} \quad (1.42)$$

it is easy to show that their effects on the output distribution is null. Therefore, the overall transfer matrix of the circuit,  $U' = C \cdot U \cdot B$ , is completely equivalent to the pure interferometer transfer matrix  $U$ .

It is convenient to further simplify the expression of  $U$  by combining all the  $N$  phase terms,  $\phi_i$ , in single term. This allows us to gather some insights on the functioning of the interferometer. The reduction procedure is straightforward and follows the steps illustrated in Figure 1.6 which allow to simplify on phase term at a time. We can

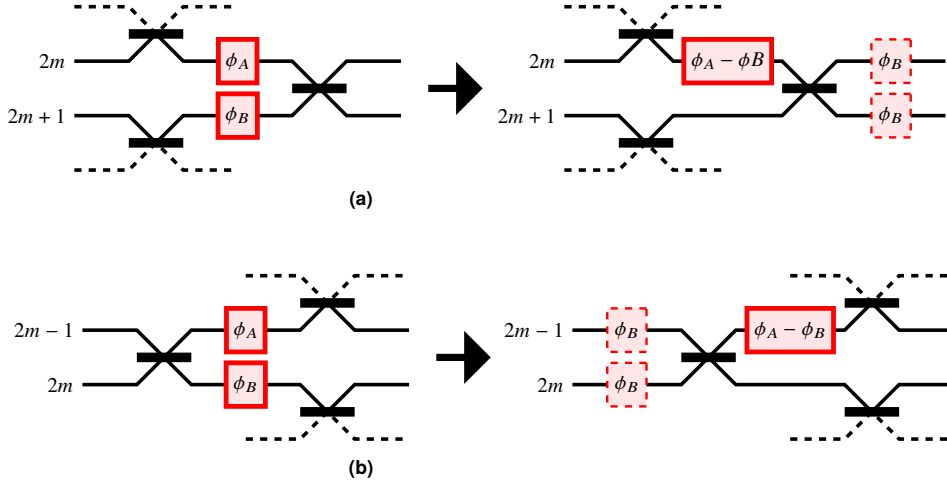


**Figure 1.6:** Procedure for the reduction of the number of phase shifters in the device. **a)** Procedure for the odd modes. The matrix of the the circuit remains unchanged by removing  $\phi_B$  if the phase term  $\phi_A$  in the mode  $2m$  is substituted with  $\phi_A - \phi_B$  and two phase shifters  $\phi_B$  are added at the outputs  $2m$  and  $2m + 1$ . The latter two can be incorporated in the  $C$  matrix whose effect is null on the output state distribution. **b)** Procedure for the even modes. The matrix of the the circuit remains unchanged by removing  $\phi_B$  if the phase term  $\phi_A$  in the mode  $2m - 1$  is substituted with  $\phi_A - \phi_B$  and two phase shifters  $\phi_B$  are added at the inputs  $2m - 1$  and  $2m$ . The latter two can be incorporated in the  $B$  matrix whose effect is null on the output state distribution.

start from the  $N$ -th mode and iterate the steps over each mode until we reach mode 1. In this way we retrieve a description of the interferometer with a single phase  $\alpha_1$  as represented in Figure 1.7:

$$\alpha_1 = \sum_{m=1}^{N/2} \phi_{2m-1} - \phi_{2m} \quad (1.43)$$

This phase term is a collective term that depends on all the modes of the interferometer. We notice that the symmetry of the circuit allow the apply the procedure starting from any mode. Obtaining  $N$  equivalent interferometers each with a single phase shifter  $\pm\alpha_1$  in mode  $j$  where the ‘+’ sign is referred to odd modes, alternatively the ‘-’ sign for even mode.

### 1.5.3 Direct multi-photon interference

First, we can prove that none of the phase shifters  $\phi_i$  influence the output state of the interferometer, in terms of detection probability, is the input Fock state has less than  $n$  photons. In fact, considering an arbitrary  $k$ -photon Fock state at the input with  $k < n$ , at least one beam-splitter of the first row will remain without any photon at the input; say the beam-splitter connecting modes  $2m - 1$  and  $2m$ . By composing an equivalent interferometer of the kind of Figure 1.7, with a single phase shifter  $\alpha_{2m}$  on the mode  $2m$ , it follows that no photon will travel through the phase shifter  $\alpha_{2m}$ , and therefore this phase shifter cannot influence the output state.

Now, we can focus on the influence of the phase  $\alpha_1$  on the photon distribution at

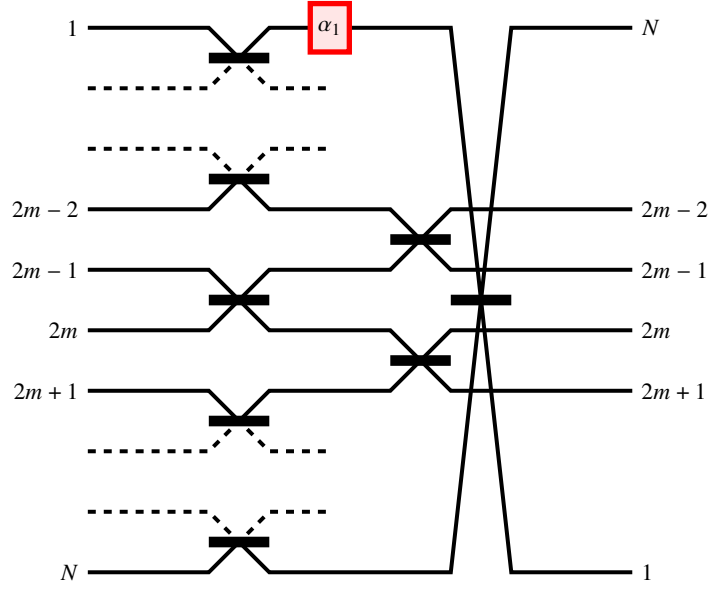


**Figure 1.7:** Scheme of the  $N$ -mode interferometer equivalent to the one in Figure 1.5. The phase shifters  $\phi_i$  are substituted with a single phase shifter  $\alpha_1$  by means of the procedure illustrated in Figure 1.6.

the output for a specific Fock state with  $n$  photons. We consider the probability of detecting, at the output, the state  $|S_{out}\rangle$  which is identical to the input state  $|S_{in}\rangle$  and in which every photon is in a different odd mode:

$$|S_{in}\rangle = |S_{out}\rangle = |S\rangle = |1, 3, \dots, N-1\rangle \quad (1.44)$$

For this particular states, the scattering matrix  $U_{S,S}$  (defined in (1.30)) can be easily computed by inspection, given the sparse connections between modes inside the interferometer. Indeed, a photon injected in an odd mode  $(2m-1)$  can exit either in the same mode  $(2m-1)$  or in the adjacent odd mode  $(2m+1)$ . In particular, such photon can reach the  $(2m+1)$ -th mode by being transmitted two times in both the first and second beam-splitter, each giving a phase term of  $e^{i\pi/2}$ :

$$U_{m+1,m} = \frac{i}{\sqrt{2}} \cdot \frac{i}{\sqrt{2}} = -\frac{1}{2}. \quad (1.45)$$

Alternatively, in the other case, the photon undergoes two reflections (both with a null phase delay), thus:

$$U_{m,m} = \frac{1}{\sqrt{2}} \cdot \frac{1}{\sqrt{2}} = \frac{1}{2} \quad (1.46)$$

and all the other terms of the scattering matrix associated to the input are null since no other modes are connected to them.

Taking into account the  $\alpha_1$  phase term in mode 1, we can write the complete scattering

matrix as:

$$U = \frac{1}{2} \begin{pmatrix} e^{i\alpha_1} & & & & & & & -1 \\ -1 & 1 & & & & & & \\ & -1 & 1 & & & & & \\ & & & \ddots & \ddots & & & \\ & & & & \ddots & \ddots & & \\ & & & & & \ddots & \ddots & \\ & & & & & & -1 & 1 \end{pmatrix} \quad (1.47)$$

### Fully indistinguishable photons

From the previous derivation, which assumed a Fock state of indistinguishable photons as input, the permanent of  $U$  can be computed by applying iteratively the Laplace formula [30] adapted for permanents obtaining:

$$\text{Per}(U) = \frac{1}{2^n} (e^{i\alpha_1} + (-1)^n) \quad (1.48)$$

and thus, the detection probability  $\mathcal{P}_{ind}$  reads:

$$\mathcal{P}_{ind} = |\text{Per}(U)|^2 = \frac{1}{2^{2n-1}} (1 \pm \cos \alpha_1) \quad (1.49)$$

where the plus (minus) sign is adopted for even (odd)  $n$ . This result indicates an interference fringe with unit visibility spanning  $\alpha_1$  in  $[0, 2\pi]$ .

### Partially distinguishable photons

We consider the situation presented in the previous section with the difference that we inject in the interferometer partially distinguishable photons. We are still injecting  $N$  photons into the odd modes and post-selecting the output state with  $N$  photons in the odd modes.

We can adopt a model similar to (1.40) to describe the density matrix of  $n$  photons [29]

$$\rho = c^\perp \rho^\parallel + \sum_i c_i^\perp \rho^\perp \quad (1.50)$$

where  $\rho^\parallel$  is the state of with all  $n$  indistinguishable photons and  $\rho^\perp$  is the state having at least two photons that are mutually orthogonal (i.e. fully distinguishable).

The probability of  $\rho^\parallel$  coincides with the probability (1.49) computed in the previous case of fully indistinguishable photons.

The probability of the remaining terms can be assessed exploiting the structure of the interferometer. Consider one of the states  $\rho_i^\perp$ , the fact that at least two terms are orthogonal implies that at least two photons injected in subsequent odd modes (say  $2m-1$  and  $2m+1$ ) are orthogonal. The distinguishability of a pair of photons implies the distinguishability of their evolution paths through the interferometer: since we can distinguish them at the input we are also able to determine if they remained in the same mode or they shifted two modes back. As discussed before, a photon can either

exit from the same odd mode it has been injected to or from the adjacent odd mode. Hence, knowing the path followed by a single photon imply a *single* possible path for all the *others* regardless of their distinguishability.

Therefore the probability of the desired output state is the same for all states  $\rho^\perp$  independently of how many and which photons are distinguishable, the distinguishability of two photons is enough to destroy all the interference.

Following this reasoning, the probability of  $\rho^\perp$  can be computed in the simplest case of  $n$  fully *distinguishable* photons:

$$\mathcal{P}_{dist} = \text{Per}(|U|^2) = \frac{1}{2^{2n-1}} \quad (1.51)$$

The overall probability reads:

$$\begin{aligned} \mathcal{P} &= c^\parallel \mathcal{P}_{ind} + \sum_i c_i^\perp \mathcal{P}_{dist} \\ &= c^\parallel \mathcal{P}_{ind} + (1 - c^\parallel) \mathcal{P}_{dist} \\ &= \frac{1}{2^{2n-1}} \left[ 1 \pm c^\parallel \cos \alpha_1 \right]. \end{aligned} \quad (1.52)$$

This expression similar to (1.49), but the visibility of the interference fringe is given by  $c^\parallel$ .

Therefore, by modifying the value of  $\alpha_1$  we are able to obtain an interference fringe whose visibility is a characterization of the *genuine* multi-photon indistinguishability.

## Chapter 2

# Femtosecond Laser Micromachining

In the seminal work [31], Davis *et al.* pioneered the use of femtosecond laser micromachining (FLM) for writing waveguides in transparent media. Since then, this technology has been employed in several applications such as realization of circuits for quantum photonics [32] and astrophotonics [33].

FLM is based on nonlinear absorption of focused laser pulses to induce a permanent localized modification in a dielectric medium. Waveguides are fabricated by tailoring the irradiation parameters to achieve a smooth refractive index change in the dielectric material, and continuous translation of the sample allows the inscription of circuit.

Over the years, femtosecond laser waveguide writing has affirmed itself as a very interesting technology in the field of integrated optics. Among the advantages, it is a mask-less procedure, not requiring the use of any lithographic step nor clean-room facilities. It allows fast prototyping of photonic circuits and, being inherently a three-dimensional technology, it allows the exploration of three-dimensional designs which would be otherwise impossible to realize with other fabrication techniques.

### 2.1 Femtosecond pulse interaction with dielectrics

Nonlinear absorption is essential for the realization of waveguiding structures since the modification of the material needs to be localized in a confined region. In order to assure such absorption regime, photon energy smaller than the energy gap of the dielectric material is needed.

Tightly focused femtosecond laser beam can achieve peak intensities of  $10 \text{ TW/cm}^2$ . These intensities are sufficient to trigger optical breakdown in dielectric media and permanent modification is achieved as a result of two subsequent processes: energy accumulation with the formation of ionized electronic plasma, and the following relaxation process in which the accumulated energy is released to the lattice.

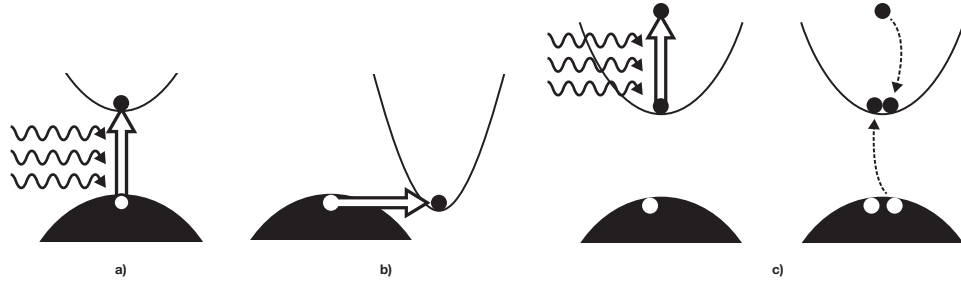


**Figure 2.1:** Schematic representation of the nonlinear absorption processes. **a)** Multiphoton absorption. **b)** Tunneling ionization. **c)** Avalanche ionization. [34]

### 2.1.1 Plasma formation

The nonlinear absorption process is typically ascribed to three possible mechanisms depicted in Figure 2.1.

#### Multiphoton absorption

Multiphoton ionization is the dominant absorption mechanism at lower intensities and high frequencies. Since the photon energy is not enough to bridge the bandgap, a valence electron is promoted to the conduction band after the absorption of  $m$  photons are absorbed such that:

$$mh\nu > \epsilon_g \quad (2.1)$$

where  $\epsilon_g$  is the bandgap energy,  $\nu$  is the photon frequency and  $h$  the Planck constant.

#### Tunnelling ionization

At higher laser intensities and low frequencies the strong field distorts the band structure and reduces the potential barrier between the valence and conduction bands. As a result, electrons in the valence band undergo a direct band transition via quantum tunneling.

Keldysh [35] showed that these two photoionization processes can be described in the same theoretical framework. The Keldysh parameter allows to draw an approximate bound between the conditions for the occurrence of such two processes. It is defined as:

$$\gamma = \frac{\omega}{e} \sqrt{\frac{m_e c n \epsilon_0 \epsilon_g}{I}} \quad (2.2)$$

where  $\omega$  is the laser frequency,  $e$  is the fundamental electron charge,  $m_e$  is the effective mass of the electron in the material,  $c$  is the speed of light,  $n$  the refractive index of the media,  $I$  is the laser intensity at the focus.

If  $\gamma \ll 1.5$  tunnelling ionization is the dominant process. Alternatively, if  $\gamma \gg 1.5$  the absorption is dominated by multiphoton absorption, while for values of  $\gamma \sim 1.5$  (which is the case for typical commercial glasses used for waveguide fabrication) the absorption process is due to a combination of the two processes.

### Avalanche photoionization

Electrons already present in the conduction band can absorb laser light by free carrier absorption. After several subsequent absorption events, an electron in the conduction band can have an energy  $\epsilon_{ele}$  such that:

$$\epsilon_{ele} > \epsilon_{cond} + \epsilon_g \quad (2.3)$$

where  $\epsilon_{cond}$  is the energy of the minimum of the conduction band. If this condition is met, the excited electron can ionize a bound electron in the valence band (by electron-electron scattering), resulting in two excited electrons at the bottom of the conduction band.

These two electrons can undergo the same mechanism of free carrier absorption and ionization of bound electrons as long as the laser field is present and strong enough, giving rise to an avalanche ionization process.

Avalanche ionization requires a sufficient number of seed electrons already present in the conduction band. These electrons can be provided by the other absorption mechanisms (namely, multiphoton and tunnelling photoionization), defect states or thermally excited impurities [36].

### 2.1.2 Relaxation and permanent modification

Several mechanisms allow the energy transfer from the free-electron plasma to the lattice. These relaxation phenomena are, ultimately, the cause of the modification of the dielectric media. The energy dissipation occurs during several picoseconds time and it is completely decoupled from the absorption mechanism, which occurs in a much shorter time scale.

The physical mechanisms involved in the modification of the media are not always fully understood.

In silica glass, one can distinguish three main types of structural changes that are dependent on the exposure parameters, described in the following.

#### Smooth refractive index change

At low pulse energies ( $\sim 100$  nJ), a smooth refractive index modification has been observed in fused silica [31] which is attributed to densification from rapid quenching of the melted glass in the focal volume [40]. This regime is the best one for waveguide writing (see Figure 2.2a) since the material keeps its transparency and optical quality. Smooth and uniform refractive index modifications are indeed required to obtain low propagation losses.

#### Birefringent refractive index change

For higher pulse energies ( $\sim 150$  nJ–5000 nJ), birefringent refractive index changes have been observed in bulk of fused silica glass. Birefringence was attributed to formation of periodic nanostructures (see Figure 2.2b) that were caused by the interaction between laser field and the free electron plasma [41]. Such a second regime

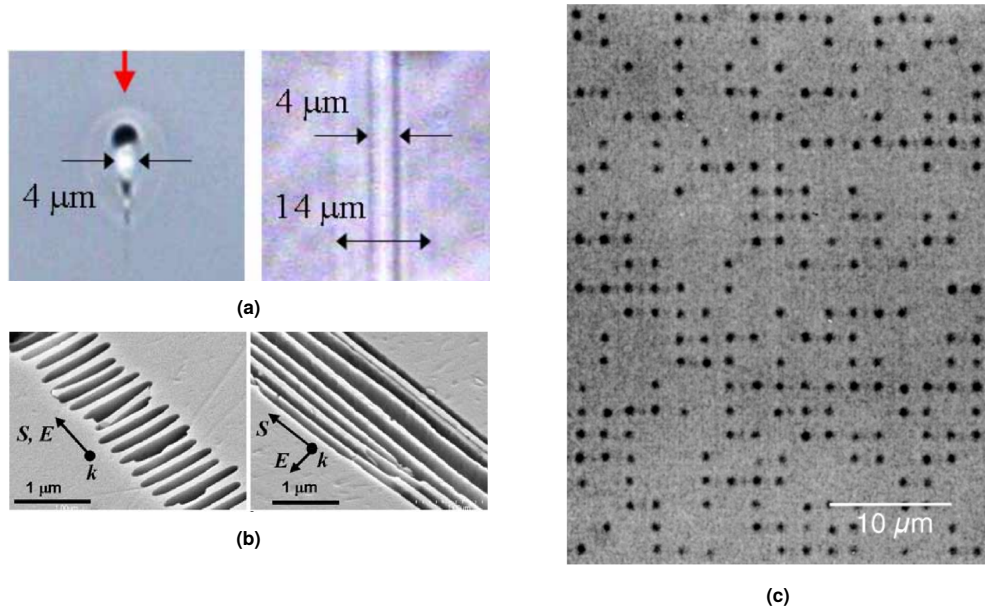


**Figure 2.2:** **a)** Transversal (left panel) and longitudinal (right panel) cross-section of a femtosecond written waveguide. Arrows indicate the guiding region ( $4\ \mu\text{m}$ ) and the surrounding cladding region ( $14\ \mu\text{m}$ ) [37]. **b)** Scanned electron microscope images of nanogratings with light polarized along parallel (left panel) and perpendicular (right panel) to the scan direction. The orientation of the grating is always perpendicular to the polarization of the writing beam. [38]. **c)** Femtosecond written binary voids in fused silica [39].

with nanograting formation is almost unique to fused silica, while it has not been observed in other kinds of substrates.

### Void formation

At high pulse energies ( $>500\ \text{nJ}$ ), where peak intensities reach  $\sim 10^{14}\ \text{W}/\text{cm}^2$ , after the electrons have transferred their energy to the lattice, high pressures are reached in the focal volume, causing the generation of shockwaves. These shockwaves leave behind a less dense or hollow (void) core, depending on the laser and material properties. Of course, by conservation of mass, this less dense region is surrounded by a shell of higher refractive index. Void structures (see Figure 2.2c) can be exploited for the fabrication of 3D memory storage [42], but are not suitable for optical waveguiding purposes.

## 2.2 Waveguide writing

### 2.2.1 Focusing conditions

Femtosecond laser pulses are focused using an optical objective in order to achieve a micrometer-sized focal spot, to drive the nonlinear absorption. In the approximation of linear propagation and absence of optical aberrations, the spatial profile of the



**Figure 2.3:** Schematic representation of the two different writing configurations. **a)** Longitudinal configuration. **b)** Transversal configuration. The arrows represent the scanning direction of the sample.

beam can be described by the paraxial wave equation and Gaussian optics. The diffraction-limited beam waist radius  $w_0$  is given by:

$$w_0 = \frac{M^2 \lambda}{\pi NA} \quad (2.4)$$

where  $M^2$  is the Gaussian beam propagation factor which gauges the quality of the beam [43],  $\lambda$  is the free-space wavelength of the laser light, and  $NA$  is the numerical aperture of the focusing objective. The Rayleigh range  $z_0$  is given by:

$$z_0 = \frac{M^2 n \lambda}{\pi NA^2}. \quad (2.5)$$

As a matter of fact, chromatic and spherical aberrations may cause a deviations in the intensity distribution near the focus, such that (2.4) and (2.5) may no longer be valid approximations. While chromatic aberrations are not problematic, given the fact that the laser is monochromatic, spherical aberrations represent a tighter limitation. Spherical aberrations are due to the spherical shape of the focusing lens. When focusing in air, the rays would converge in a single point, on the other hand, by focusing under the surface of glass, the rays will converge in a bigger volume because of the Snell laws at the interface. In glass-written waveguides, spherical aberrations are introduced by the index mismatch at the air-glass interface and, as a result, waveguides properties are strongly depth dependent.

To cope with spherical aberrations, one can use a particular objectives with correction collar, designed for the compensation of the aberration at a given depth which can be set by the experimenter. An alternative solution is given by the use of an immersion objective. Such objective is conceived to work immersed in oil or water in order to reduce the index mismatch and diminish the effect of spherical aberrations.

### 2.2.2 Writing configuration

Two possible configurations, adopted for femtosecond laser waveguide writing, are showed in Figure 2.3. In the longitudinal writing configuration, the sample is scanned along the parallel direction with respect to the incident beam. This configuration, given the transversal symmetry of the Gaussian intensity profile of the beam, provides waveguides with intrinsic a cylindrical symmetry. The main disadvantage is

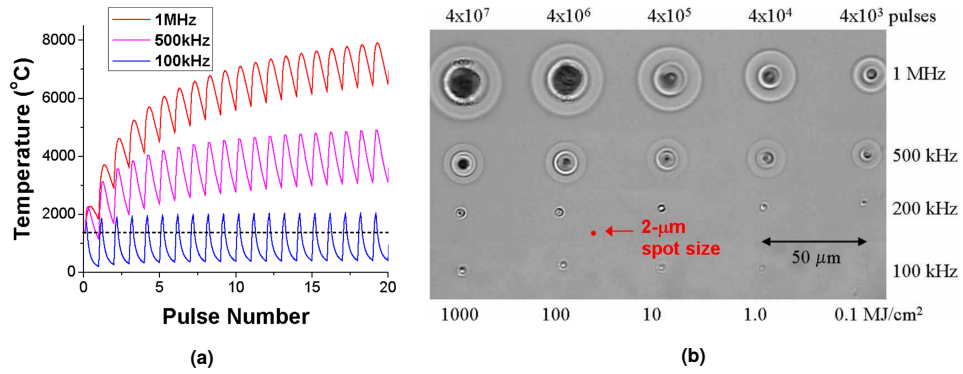


**Figure 2.4:** **a)** Numerical model of glass (Schott AF45) temperature versus exposure; the three different regimes are highlighted: low (blue), intermediate (magenta) and high (red). **b)** Optical microscope image showing the increasing of the modified region for different values of repetition rates (rows) and exposures (columns). [37]

that the writing length is limited by the working distance of the lens, which is typically less than a few centimeters.

In the transverse writing scheme, the sample moves perpendicularly to the laser beam. In this configuration, the working distance of the focusing objective does not limit the length of the waveguides, and optical structures can be fabricated with sufficient flexibility in a depth range of several millimetres, allowing the realization of three-dimensional structures. The disadvantage of this scheme is that the cross-section of the waveguide can be asymmetric due to the non unit ratio between depth of focus and spot size:

$$\frac{z_0}{w_0} = \frac{n}{NA}. \quad (2.6)$$

Objectives employed for waveguide writing have typical  $NA$  values in the range 0.25–0.85. If the refractive index is the one of glass  $n = 1.5$ , the focal volume asymmetry  $n/NA$  varies between 1.8 and 6.0. The aforementioned asymmetry may result in waveguides with elliptical modes that couple poorly with standard single-mode fibres. This problem can be overcome by the use of beam-shaping techniques [44, 45] or by exploiting thermal accumulation effects (see the following Section 2.2.3).

### 2.2.3 Repetition rate and thermal effects

The repetition rate of the laser is one of the main experimental parameters that influence the characteristics of the waveguide. One can distinguish two main regimes: low and high repetition rates.

At low repetition rates (typically below 250 kHz), the time interval between two subsequent femtosecond pulses is higher than the heat diffusion time in the dielectric media (which is of the order of 1  $\mu$ s). Therefore, material modifications depend on a single pulse, since the lattice has already undergone a full thermal relaxation when the next pulse impinges on the material. Waveguides fabricated in this regime may present significant coupling losses and birefringence, with an optical mode that is asymmetric. Moreover, the low repetition rate often requires low writing speeds

( $\sim 0.1$  mm/s), in order to deposit enough energy into the dielectric material, which results in a long fabrication time.

On the other hand, at high repetition rates (above 2 MHz) the time interval between two subsequent pulses is smaller than the heat diffusion time. As a result, the effects of different pulses pile up in the focal point, generating a strong heat accumulation (right panel of Figure 2.4) Even with a very small focal spot size, heat diffusion generates a much larger and isotropical modification.

Actually, one can consider also an intermediate regime (see Figure 2.4), with repetition rates that range between hundreds of kHz and few MHz. Gradual heat accumulation effects allow to obtain waveguide with a symmetric and uniform structure while maintaining a cross-section which is comparable to the beam waist of the impinging beam. The advantages of high and low repetition rate regimes combine making this intermediate regime one of the most interesting for femtosecond laser waveguide writing.

### 2.2.4 Annealing process

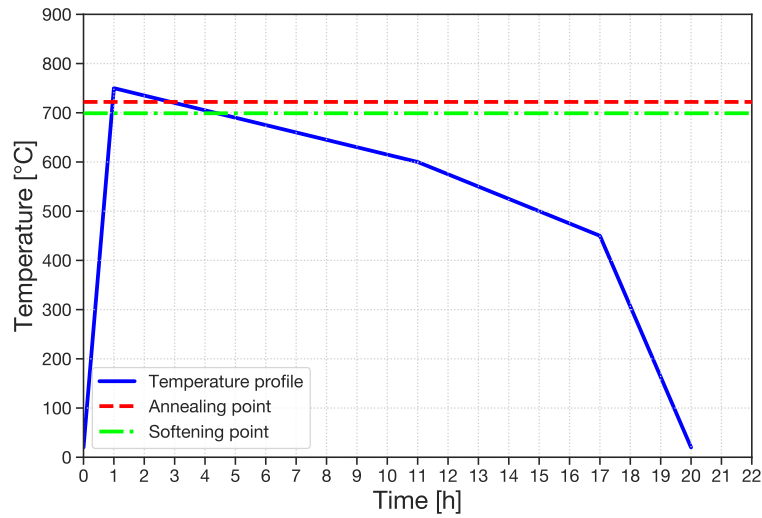
As discussed in the previous section, thermal phenomena play relevant role in the femtosecond-laser modification processes. In particular, material can locally reach the melting point and, subsequently, resolidify upon cooling. During this process, however, mechanical stresses can accumulate.

Thermal treatments are commonly employed in glass manufacturing in order to reduce such stresses. A study of the temperature dependence of the properties of glass allow to understand how thermal treatments works. Here are listed, the most important characteristic temperatures:

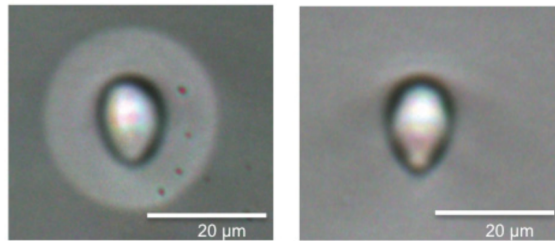
- *Strain point*: temperature at which the glass is still solid and keeps its shape, but internal stresses are released in few hours.
- *Annealing point*: temperature at which the internal stresses are released in several minutes.
- *Softening point*: at this temperature the glass is soft enough to deform under its own weight.
- *Working point*: the glass is sufficiently soft to be shaped by blowing.

A thermal annealing process consists in a rapid heating of the medium slightly above the annealing point, so to achieve a rapid release of the internal stresses. After a short period of time (some minutes are sufficient) temperature is reduced below the strain point and, over several hours, is brought to ambient temperature so to have a uniform cooling of the sample.

Effects of the annealing process on refractive index profile and bending losses of femtosecond-written waveguides were first investigated by Arriola *et al.* [46]. They proposed a two-steps fabrication process for low-losses waveguides at 1550 nm written in boro-aluminosilicate glass (EAGLE 2000, Corning). The first step consists in writing *multimode* waveguides using low transition speed and high pulse-energy (500 mm/min and 90 nJ, respectively). At this stage, microscope images of the



(a)



(b)

**Figure 2.5:** **a)** Annealing recipe for EagleXG (Corning) borosilicate glass. Horizontal lines represent respectively the annealing point (AP) at 722 °C and the strain point (SP) at 699 °C. **b)** Cross-sections of a waveguide before (left panel) and after (right panel) the annealing process.

waveguides cross-sections reveal the presence of a solidified core surrounded by an outer ring modification (see left panel of Figure 2.5b). After the fabrication, follows the annealing process (Figure 2.5a) which releases the stress accumulated in the material due to the high energy deposition. As a result, the outer modification ring is almost totally removed (see Figure 2.5b, right panel) and one measures single mode operations.

In the same work, the authors mention that the annealing process is beneficial to reduce the birefringence of the waveguides, since this features mainly arises from stress accumulation in the material.

### 2.3 State of the art

Femtosecond laser written waveguides are characterized by a low index contrast ( $\Delta n \approx 0.01 - 0.001$ ) similar to those of standard optical fibers, thus allowing efficient fiber-waveguide coupling. Combing these characteristics with the fast prototyping

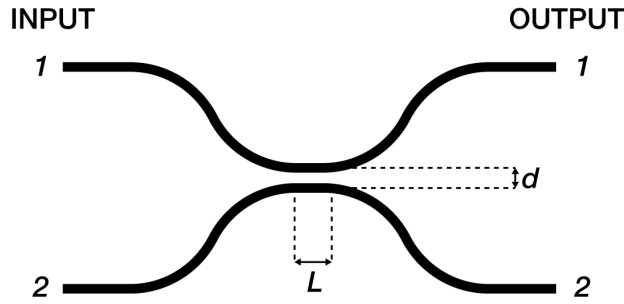


**Figure 2.6:** Schematic representation of the directional coupler. Two far-apart waveguides are brought together in the interaction region permitting power exchange via evanescent coupling and then they separate again.

and 3D capabilities, FLM has affirmed itself over the years as a viable technological platform for the fabrication of integrated optical circuits. This section focuses on the state of the art of passive and reconfigurable femtosecond laser written photonic devices.

### 2.3.1 Passive integrated photonic circuits

#### Directional coupler

A fundamental building block for integrated optical circuits is the directional coupler (Figure 2.6). It is employed in several applications, [47] and is the basic component for Mach-Zender and more interferometers for sensors [48].

In a directional coupler, two waveguides are brought close together permitting power exchange between them through the evanescent coupling mechanism. Assuming (for simplicity) single-mode waveguides, the sustained mode has a Gaussian shape with exponential tails outside the core [49]. When the waveguides are sufficiently close to each other, the overlap of the exponential tails can be non-negligible and it can be shown [49] that the power exchange between the waveguides has a sinusoidal behaviour as a function of the coupling length. In the particular case in which the two waveguides are identical and the initial power is localized in the first waveguide, the power exchange as a function of the propagation coordinate  $z$  is given by:

$$\begin{cases} P_1(z) = P_1(0) \cos^2(kz) \\ P_2(z) = P_1(0) \sin^2(kz) \end{cases} \quad (2.7)$$

where  $P_{1(2)}(z)$  is the power in the first (second) waveguide and  $k$  is the coupling coefficient. A complete power transfer is reached at  $z_m = \frac{\pi}{2k}(2m + 1)$  where  $m$  is an integer value.

One can engineer the waveguide distance and the interaction length, namely the length of the segments of waveguides when they are close together, to achieve the desired exchange ratio.

The first demonstration of fabrication of directional coupler using FLM is due to Streltsov *et al.* [50]. We review in the following a few of the most recent advances, regarding polarization-insensitive directional couplers, which are devices meant to

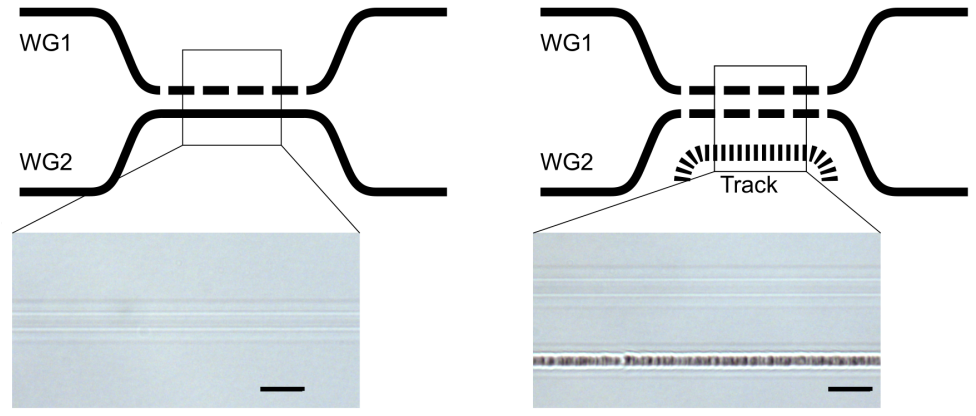


**Figure 2.7:** Schematic of the directional coupler fabricated by femtosecond laser micromachining. On the left the device proposed in [51] in which the second waveguide modifies the birefringence of the first one. On the right the scheme and microscope picture of the symmetric polarization-insensitive directional coupler proposed in [52]. The addition of a damaged track next to the second waveguide allows to equalize the birefringence. [52]

split orthogonal polarization equally. The matching condition between the two polarizations was achieved in Ref. [51] by Pitsios *et al.*, exploiting the stresses introduced during the writing process. Indeed, by writing two waveguides very close to each other, the inscription of the second guide affects the optical properties of the first one, altering the coupling coefficients for the two directions of the polarization,  $k_H$  and  $k_V$ . An optimization of the coupling distance between the waveguides permits to achieve a device with  $k_H = k_V$  and, therefore, a splitting ratio which is insensitive to the polarization.

However, that device produces two slightly different rotations of the polarization state when entering different inputs, even if the power splitting ratio is the same. In 2018, Corrielli *et al.* [52] proposed an implementation for a symmetric polarization-insensitive directional coupler (SPIDC). The idea is to extend the concept of Ref. [51] introducing an additional, non-guiding modification that affects the properties of the second waveguide (see Figure 2.7). To avoid coupling between the added track and the second waveguide, the former is written with the same irradiation parameters but with slower translation speeds. By optimizing the distance between the additional track and the second waveguide, a perfect condition between the two inputs can be achieved.

An alternative method for the fabrication of SPIDC, suggested in the same work, involved the use of annealed waveguides. Such waveguides were characterized by low propagation losses (below 0.3 dB/cm) and a birefringence value of about  $1.2 \times 10^{-6}$  which is remarkably smaller than typical values measured in femtosecond written waveguides [53]. Then, the authors proceed with the fabrication of several directional coupler with various coupling distances and interaction length finding an average difference in transmissivity between the two polarization  $\epsilon = |T_H - T_V|$  of about 0.7%, which is negligible for many applications.

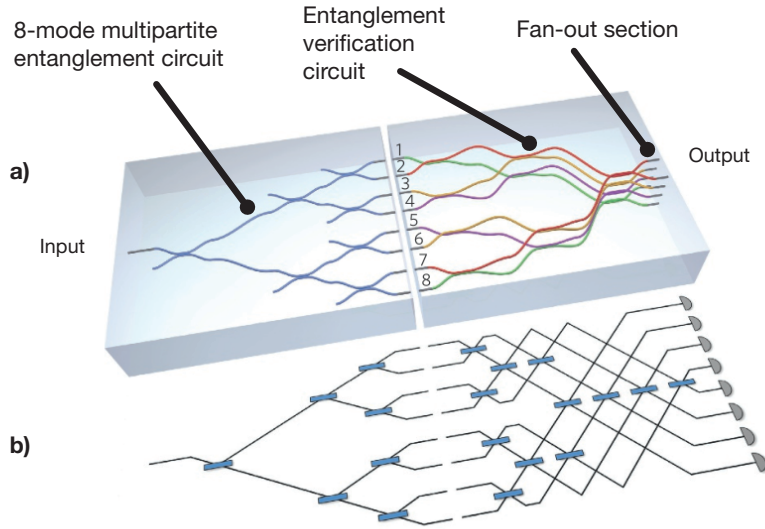


**Figure 2.8:** **a)** Integrated design of the circuits for generation and verification of 8-mode multipartite entanglement. The interferometers for the generation and verification of the entanglement are implemented in two different circuits. **b)** Theoretical scheme of the devices realizing generation and verification of 8-mode multipartite entanglement. Image modified from [54]

### Passive interferometric circuits

Directional couplers are also the building components for high-complexity interferometric circuits with large number of modes. In the following, we will present three examples.

Szameit *et al.* experimentally realized an integrated optical circuit for generation of high-order W-states, which are quantum states where one single photon is coherently distributed among  $N$  spatially separated modes [54].

The authors fabricated interferometers to generate W-states spanning  $N = 2, 4, 8$  and 16, using femtosecond laser micromachining in fused silica substrates. The circuit is constituted by a network of cascaded 50:50 directional couplers allow the synthesis of the 2-, 4-, 8-partite W-state selecting an appropriate input channels. The scheme of such integrated platforms is shown in Figure 2.8.

In the same work, the authors realized an integrated interferometer for the verification of the multipartite entanglement which is to be placed in conjunction with the entangling-circuit presented above. In particular, a circuit for the characterization of the 8-modes W-state was experimentally realized. The interferometer comprises 12 directional couplers, written in three-dimensional fashion (see Figure 2.8). For the case of  $N = 8$  the authors measured a fidelity of 91.8% between the output mode and the target  $|W_8\rangle$ , verifying the entanglement among all modes.

Crespi *et al.* realized an integrated photonic circuit to implement a small instance of the boson sampling problem; in particular, they studied three-photon interference in a five-mode interferometer [8]. The interferometer was written in borosilicate glass

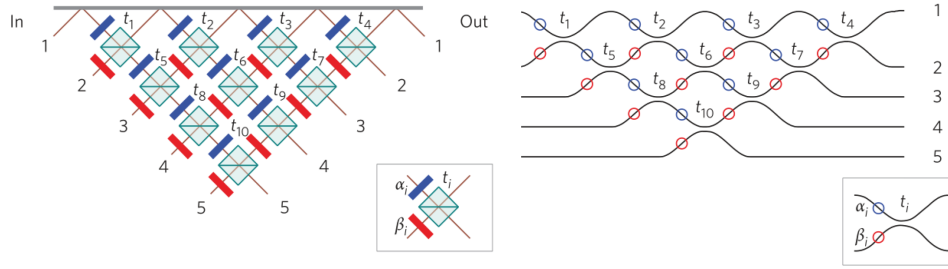


**Figure 2.9:** (Left panel) Decomposition scheme of a unitary matrix in series of directional couplers and phase-shifters. (Right panel) Integrated implementation of the scheme presented in the left panel. The circuit comprises five modes, ten directional couplers and ten phase-shifters.[8]

(EAGLE2000, Corning) and its layout is reported in Figure 2.9.

The main challenge was the independent control of the transmissivity and of the phase shifts throughout the network of directional couplers. A smooth deformation of the S-bent waveguides, stretching the optical path provided controlled phase-shifters, while out-of-plane rotations of one arm of the directional couplers (exploiting the 3D capabilities of the technology), controlled the transmissivity of the directional couplers without other geometrical alterations.

The final circuit had a footprint of 42 mm×0.7 mm with input-output transmission of appropriately 5 dB. With this device, authors were able to confirm the so-called “permanent formula” that governs the multiphoton scattering for up to three photons. In the following years, the same group introduced a novel methodology for implementation of Fourier interferometers [24]. The authors fabricated Fourier interferometers in borosilicate glass (EAGLE2000, Corning) with 4 and 8 optical modes and propagation losses of 0.5 dB/cm.

The scheme of the two devices is given in Figure 2.10. They are composed of a complex network of 3D directional couplers, with proper interaction length and coupling distance in order to achieve balance splitting, and phase-shifters, implemented with smooth deformation of the S-bends.

The fidelity between the theoretical Fourier unitary matrix and the transformation matrix of the chip is  $\mathcal{F} \approx 98.2\%$ , confirming the high quality of the fabrication process. The chips were used for 1- and 2-photon experiments for observation of the suppression law[13].

### 2.3.2 Reconfigurable integrated photonic circuits

Reconfigurability has many advantages in integrated optics. It can be used, for example, to compensate for imperfections due to fabrication tolerances [55], or to reconfigure the transfer matrix of a device, thus allowing to perform different experiments with a single chip [56].

The possibility to dynamically reconfigure the behaviour of integrated optical circuits can be achieved with thermo-optic phase-shifters, which exploit the dependence of the refractive index on the temperature. Experimentally, thermal phase-shifters are

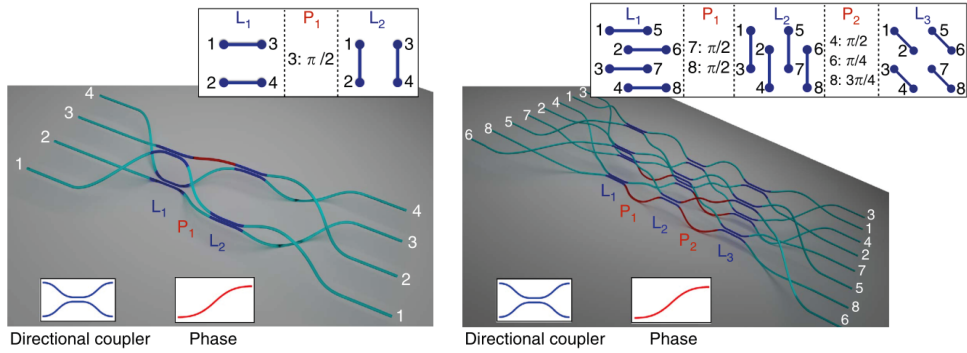


**Figure 2.10:** Layout of the  $m = 4$  (left panel) and  $m = 8$  (right panel) interferometers. The  $m = 4$  device comprises four directional couplers and a single phase-shifter (as indicated on the top-inset) while the  $m = 8$  device has a much more complex structure, with twelve directional couplers and five phase-shifters. These interferometers are realized exploiting three-dimensional capabilities of femtosecond laser writing.[24]

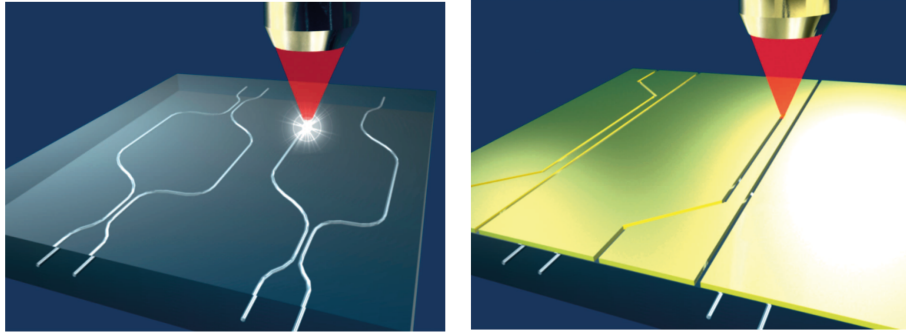


**Figure 2.11:** Schematic of the reconfigurable Mach-Zender interferometer. The Mach-Zender interferometer is written on the glass substrate using FLM (left panel). After the deposition of the gold layer, the resistors are inscribed using the same femtosecond laser system (right panel). [57]

realized by patterning thin stripes of a metallic film deposited on top of the substrate. By injecting a current in these resistive paths, one can locally vary the temperature of the substrate by Joule heating.

The first work which featured a reconfigurable femtosecond laser written circuit is due to Flamini *et al.* [57]. The authors fabricate a Mach-Zender interferometer (see Figure 2.11) in alumino-borosilicate glass, with a thermal phase-shifter placed on top of one arm. The resistor was patterned on a gold layer, using the same femtosecond laser system used for inscription of the waveguides. The device was characterized optically with one- and two-photon inputs.

In the following years, several works developed and improved the performances and the fabrication process of thermal phase-shifters allowing the realization of more complex devices. Dyakonov *et al.* [58] realized an integrated optical circuit using FLM capable of realizing any  $4 \times 4$  unitary transfer matrix. The device is fabricated in fused silica, waveguides were written  $20\mu\text{m}$  below the surface to ensure a fast

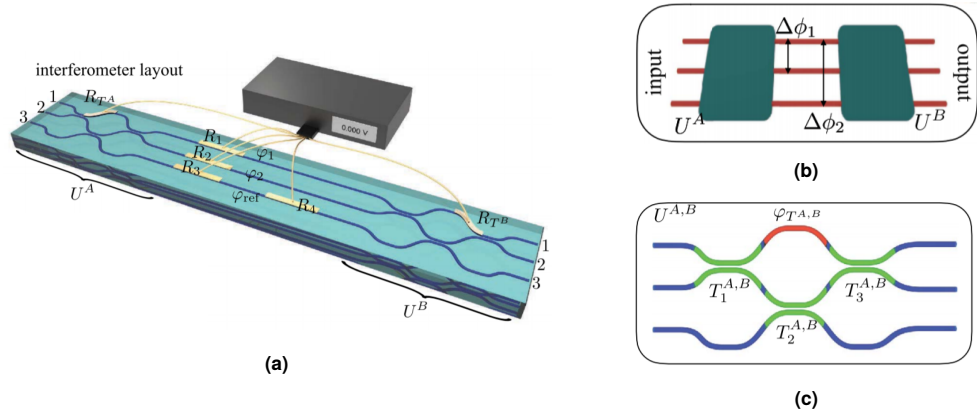


**Figure 2.12:** **a)** Complete scheme of the reconfigurable chip for multiphase estimation. **b)** Conceptual scheme of the experiment. Matrices  $U_A$  and  $U_B$  are represented as black boxes, in between them are pictured the two phase controls. **c)** Circuitual scheme of matrices  $U_A$  and  $U_B$ . Three beam-splitters and a dynamically reconfigurable phase  $\phi_T^{A,B}$ . By appropriately tuning  $\phi_T^{A,B}$ , the two multiport splitters can be set to operate as balanced tritters.

thermo-optic response. The inscribed waveguides exhibit 0.8 dB/cm propagation losses and high bending radii (80mm) which are required in order to make bending losses negligible. The heating elements are patterned in a 1  $\mu\text{m}$  thick NiCr film. To enhance the adhesion properties of the substrate, the sample was pre-heated before the film deposition.

The authors improved the switching time with respect to previous work, reaching  $\sim 10\text{ms}$ . On the other hand, they reached a  $2\pi$  phase shift upon dissipating a conspicuous amount of electrical power, which is of the order of few Watts.

In 2019, Polino *et al.* [59] realized a reconfigurable integrated optical chip for multiphase estimation. The circuit is made of three macro components (see Figure 2.12): a unitary matrix transformation  $U_A$ , acting on the input stage, an intermediate state in which four phase-shifters allow the independent control of two phase terms and, finally, another matrix  $U_B$  which produces the output state. Both matrices are realized with the same layout (see Figure 2.12c) with one phase-shifter that allow to reconfigure the unitary transformations  $U_{A,B}$ .

The device is written in borosilicate substrate (EagleXG, Corning) and exhibits propagation losses lower than 0.8 dB/cm. Thermal shifters are fabricated on top of the chip following the procedure presented in Ref. [57]. A uniform gold layer of  $\sim 60\text{ nm}$  is deposited on top of the sample, and patterned via femtosecond laser writing, obtaining resistance values in the range  $60\div 100\ \Omega$ .

Ceccarelli *et al.* [60] further improved the fabrication technique of thermo-optic phase-shifters.

In that work, the metallic film is built of a double layer of chromium and gold. Gold is the material of choice for the fabrication of thermal shifters. However, the adhesion of the gold to the glass substrate is particularly weak. To overcome this issue a thin (2 nm thick) chromium film is deposited between the glass and the gold layer to improve adhesion.

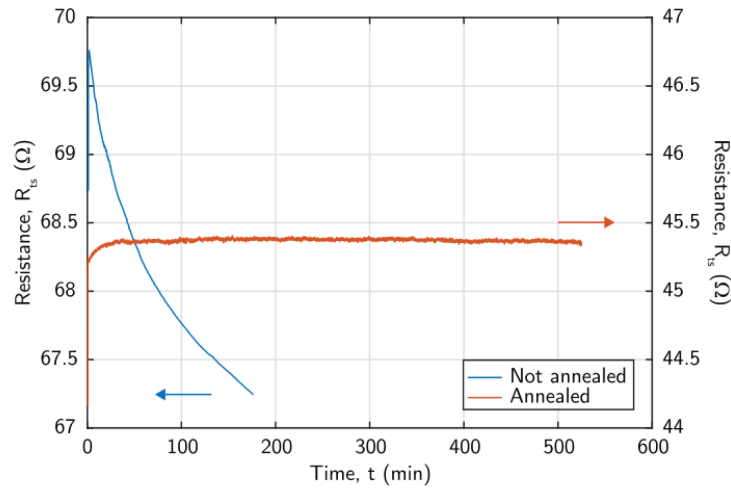


**Figure 2.13:** Comparison between the temporal stability of annealed and not-annealed thermal shifters. The resistors that have not been annealed (blue trace) have high resistance, but stability over time is an issue. On the other hand, the annealed resistors (red trace) have lower resistance with respect to the other ones, but after the initial transient the variations of the film resistances are below 0.1 % [60].

Moreover, an annealing process is tailored specifically to improve the film stability and ensure stable performances of the resistors over a long period of time, without affecting the optical properties of the waveguides. The annealing process consists of three steps: first temperature is raised with a ramp 10 °C/min up to 400 °C, then the temperature remains stable at 30 min and, at the end, the temperature is brought to ~ 20 °C in 15 h. Being the maximum temperature of the process far from the strain temperature of glass, the substrate remains unaffected by the procedure.

The annealing procedure substantially reduces the overall resistance of the metallic film (almost a factor of 2), and improve the stability over several hours of operation (see Figure 2.13).



## Chapter 3

# Experimental Methods

### 3.1 Waveguide writing setup

#### 3.1.1 General scheme

A schematic representation of the fabrication setup is shown in Figure 3.1. The setup can be divided in three block: the laser source, the beam steering and manipulation part and the motion stages, that allow to move the sample with respect to the laser focus enabling the fabrication of the devices.

Following the path of laser beam, which is emitted by a commercial femtosecond laser source (see Section 3.1.2), and goes through an attenuation stage made of two rotating  $\lambda/2$  plates and a polarizing beam-splitter. The first waveplate is actuated by a miniature gear-driven rotary stage (AEROTECH MPS75GR), while the second one is manually controlled.

Using mirrors, the laser beam is lifted from the optical table and focused using a microscope objective. In our experiments, we used a 20X Water Immersion objective (ZEISS), with  $NA=0.5$ . The glass sample is fixed to a custom-made holder, that is filled of deionized water and mounted on a gimbal adjuster. The alignment is performed with the aid of a CCD camera (Edmund Optics) that collects back-reflected light from the sample. Moreover, both the sample and the objective have been mounted in translational stages for precise control of their position during the fabrication Section 3.1.3.

A powermeter (Ophir Nova II) can be inserted in the line, before the objective, to measure the beam power.

#### 3.1.2 Laser source

The laser source used is a compact commercial femtosecond laser system, named PHAROS, produced by Light Conversion. The system consists of a Kerr lens mode-locked oscillator, a regenerative amplifier and a stretcher/compressor module.

The oscillator delivers a 76 MHz pulse train with a duration  $< 80$  fs. The gain medium is a Yb:KGW (ytterbium, doped potassium gadolinium tungstate) crystal, directly pumped by laser diodes, and the laser cavity is a monolithic aluminium block to ensure stability.

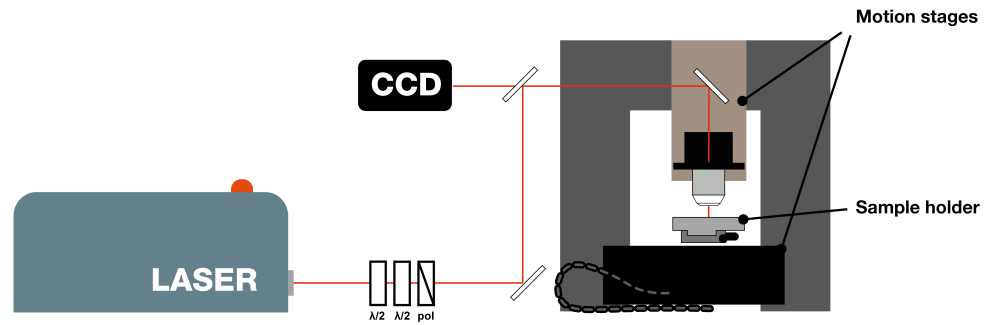


Figure 3.1: Schematic representation of the fabrication setup.

The amplification of the pulse is based on the chirped pulse amplification (CPA) technique, which allows to obtain femtosecond pulses with high peak intensity. The CPA process is composed by a first stage that stretched the pulse in the temporal domain; this is followed by an amplification stage and, finally, by the back-compression of the pulse duration.

The stretcher/compressor module is based on a single diffraction grating that can be adjusted to introduce positive or negative chirp, which can be used to tune the pulse width. The regenerative amplifier, is based on a Yb:KGW crystal, pumped by two continuous wave solid state laser diodes.

The system outputs sub-190fs pulses with a centre wavelength of  $1028 \pm 5\text{nm}$  and a maximum pulse energy of 0.2mJ. The repetition rate can be tuned from single-shot to 1MHz.

### 3.1.3 Motion stages

The motion stages consist of three independent, linear translators along the  $x$ ,  $y$  and  $z$  directions. The motion stage that control the position along the  $z$ -coordinate (AEROTECH ABL1500Z-050), changes the position of the objective and allows to move the position of the focus depth inside the substrate during the fabrication. This stage has a maximum travel range of 50mm with a nominal resolution of 1 nm and maximum speed and acceleration that are 300mm/s and  $20\text{m/s}^2$ , respectively. The other two stages (AEROTECH ABL1500WB-200, for the  $x$ -direction, and AEROTECH ABL1500-100 for the  $y$ -direction), move the sample in the plane perpendicular to the laser beam. Maximum travel ranges are 100 mm and 200 mm, respectively for  $x$  and  $y$  direction, with a nominal 1 nm resolution. Maximum velocity and acceleration, identical for both stages, are 2m/s and  $20\text{m/s}^2$ .

The motion stage drivers also feature a TTL output that is fed to the laser allowing a synchronized shuttering of the beam.

The stages are controlled by a computer equipped with a proprietary software (AEROTECH CNC Operator Interface) and can be programmed using G-code scripts.

## 3.2 Chip post-processing

### 3.2.1 Glass polishing

Light coupling with femtosecond written waveguides strongly depends on the conditions of the facet. Oftentimes, after waveguide fabrication, the input and output sides present glass chipping, surface defects and roughness. Surface polishing of the glass facets is ordinarily performed, to reduce the scattering losses, and enhance coupling efficiency.

This process is done by means of a polishing machine, which uses moving abrasive disks. The sample is mounted perpendicularly with respect to the moving disk and, by using a sequence of abrasive disks with decreasing roughness, one can reach optical-grade polishing.

### 3.2.2 Gold coating and resistor patterning

Fabrication of the thermo-optic phase-shifters follows the procedure of Ref. [60] (see also Section 2.3.2). The deposition of both chromium and gold films is performed at the PoliFAB laboratories, using a magnetron sputtering system (Leybold LH Z400). After the film deposition, the sample undergoes a thermal annealing process and then, resistors are patterned using the same femtosecond laser system used for inscription of the waveguides.

The gold layer is inscribed by superficial ablations, that allow a precise removal of the metallic film, using a 10X microscope objective with  $NA=0.25$  (Leitz-Wetzlar), an irradiation power of 200 mW and a translation speed of 2 mm/s. Moreover, the contours of the microheaters were ablated 3 times with an offset of 1  $\mu\text{m}$  between each inscription to increase the width of the ablated mark and improve the isolation between the conductive tracks.

The thin resistive stripes have to be inscribed on top of the waveguides. In order to have a precise alignment with the underlying optical circuit, multiple markers are realized on the surface of the glass sample when the waveguides are fabricated. These markers are imaged by collecting the back-reflection of the laser beam on the CCD camera of the fabrication setup, the retrieval of their positions allows to align the reference frame defined in different fabrication steps.

Since conventional soldering techniques would irreversibly damage the delicate metallic film, electrical connections are realized by bonding the gold pads with standard electrical pin headers (2.54 mm pitch), by means of an epoxy electrically-conductive glue.

### 3.2.3 Fiber pigtailling

Fiber pigtailling consists in permanently coupling fiber arrays to the input and output ports of the integrated optical device, to allow easy interfacing with external sources, detector or other external devices via standard optical connectors. Fiber arrays are compact devices for holding multiple bare fibers, which are mounted side by side on V-grooves (as shown in Figure 3.2) and kept at a fixed pitch. At the other end, optical fibers have standard fiber connectors.

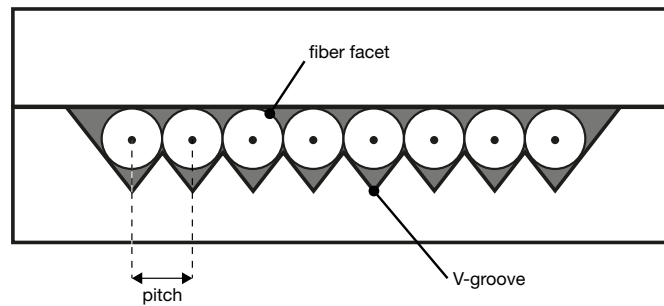


**Figure 3.2:** Schematic representation of a fiber array input facet. The V-groove keeps eight fibers at a constant pitch, the fibers are clamped in place by two pieces of glass.

During the design phase of the waveguide circuit, the pitch of adjacent modes is chosen in order to match the one of the V-groove. Moreover, fiber arrays have to be carefully chosen for the specific wavelength of the experiment, in order to minimize the coupling losses with the inscribed waveguides.

The fiber array is mounted in a specific fiber holder and is manoeuvred using sub-micrometric manipulators, allowing a precise control of the three spatial coordinated and the three rotational angles for maximizing the light coupling with the chip. Once the optimal coupling is achieved, the fiber array is glued to the glass substrate using UV-glue.

### 3.3 Characterization methods

#### 3.3.1 Microscope inspection

After laser irradiation, the glass sample is visually characterized with a microscope, to evaluate the outcomes of the fabrication or glass-processing operations.

A top view of the glass sample allows to check the overall geometry of the fabricated waveguides, or detect damages and interruptions of the irradiated tracks. These interruptions cause high losses and, in some cases, impair the guiding properties of the inscribed structures. They are usually caused by presence of particles, e.g. dust, on the fabrication surface that locally distort the laser focus.

Inspection of the lateral facets allows to check the quality and roughness of the input/output interfaces. This check is especially useful after the polishing step, or for a visual analysis of the waveguides cross-sections. The latter procedure is also useful to compare cross-sections when waveguides are written with different irradiation parameters, or to draw comparison between structures before and after annealing process.

All the aforementioned characterizations are performed using a Nikon ECLIPSE ME600 microscope equipped with a PixeLINK PL-B871 CCD camera for images acquisition. The microscope mounts four different objectives: Nikon Plan Flour 4X, 10X, 20X and 40X.

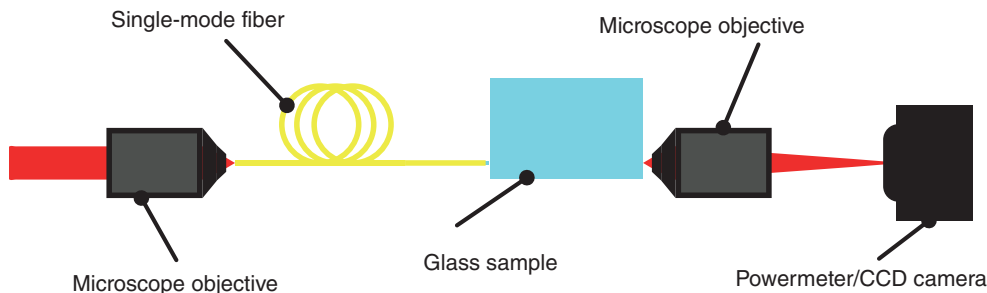


**Figure 3.3:** Scheme of the end-fire configuration for coupling light into the fabricated devices.

### 3.3.2 Optical characterization setup

The optical properties of the waveguides are characterized by coupling classical light. These measurements assess the polarization response of the circuits, the mode profile, losses of the waveguides and the power distribution at the output ports.

Coherent light used for characterization is produced by laser diodes with wavelength ranging from 904 nm to 940 nm.

All the optical characterization measurements reported in this Thesis are performed adopting the so-called fiber coupling (or *end-fire* coupling) configuration. It consists of coupling light into the integrated optical device directly from an optical fiber, by aligning the distal end of the fiber with the input facet of the waveguide.

First of all, the free-space coherent light emitted by the laser source is couple to a single mode waveguide using a microscope objective. The other end of the fiber is peeled and cleaved and the fiber tip is brought as close as possible to the input of the integrated waveguide, to maximize the coupling.

The light coming out of the integrated circuit is collected by an objective and focused on a power-meter (Ophir, NovaII or Anritsu ML9001A) or a CCD camera (Edmund OpticsEO-1312M). The end-fire coupling configuration is schematized in Figure 3.3. The relative positioning of the sample and the fiber tip are controlled using a sub-micrometric positioning system: Melles Griot NanoMAX stages are used for the fiber and the objective, while the sample is mounted on a four-axis micropositioner Thorlabs MBT40.

An alternative setup is also available, based on two six-axis hexapods (PI H-811), one for the input fiber and one for the collection objective. The hexapods are computer controlled, enabling precise and granular control over the movements of the two positioning systems. This setup is particularly useful for characterization of large integrated devices with regular pitch between waveguides, or to perform the fiber pigtailling process (see Section 3.2.3).

In this case, the sample is mounted on a manipulator with two linear axes and three rotational axes to ensure correct positioning and leveling. An optical zoom camera (Opto 100-ZOS7-25) is used to control the sample position and the relative distance between the bare waveguide tip and the input facet.

### 3.3.3 Mode profiling

Measures of the mode profile give information on the confinement properties of the waveguides.

The waveguide is coupled using an end-fire configuration, and the end facet of the fiber and of the waveguide are imaged on the CCD camera. Taking care of not saturating the sensitive pixels, the images of the modes are acquired using the CCD proprietary software.

Mode profiling is useful to measure the size of the femtosecond laser written waveguides, to evaluate the symmetry of the waveguide, and allows to discriminate between single or multi-mode behaviour and estimate coupling losses (see Section 3.3.4).

### 3.3.4 Losses characterization

Light propagation in waveguiding structures introduces losses. Their characterization is fundamental in any photonic application, even more when dealing with quantum photonics experiments which are based on single photons inputs.

The characterization of femtosecond laser written waveguides is performed using the apparatus presented in Section 3.3.2.

First, one measures the total losses introduced by the device, comparing input and output power. This term is called insertion losses (IL) and defined as:

$$IL|_{\text{dB}} = 10 \log_{10} \left( \frac{P_{in}}{P_{out}} \right) \quad (3.1)$$

where  $P_{in}$  is the measured output power from the optical fiber,  $P_{out}$  is the measured output from the waveguide or photonic device.

The Insertion Loss is the results of several different contributions:

- *Fresnel Losses* (FL), are losses due to the refractive index mismatch at the air-glass interface, where a portion of light is back-reflected. In case of normal incidence (as it is the case of all the measurements in this Thesis) one can estimate the reflectance of the interface as:

$$R = \left( \frac{n_{glass} - n_{air}}{n_{glass} + n_{air}} \right)^2 \quad (3.2)$$

where  $n_1$  and  $n_2$  are the refractive indices of the two media. The Fresnel losses result to be:

$$FL|_{\text{dB}} = -10 \log_{10} \left( \frac{P_{out}}{P_{in}} \right) \quad (3.3)$$

$$= -10 \log_{10} \left( \frac{(1 - R)P_{in}}{P_{in}} \right) \quad (3.4)$$

$$= -10 \log_{10} (T) \quad (3.5)$$

where  $T$  is the interface transmittance defined as  $T = 1 - R$ .

- *Coupling losses* (CL), are losses due to the mismatch between the modes of the optical fiber and of the femtosecond laser written waveguide if both of them are single-mode.

$$CL|_{\text{dB}} = -10 \log_{10} \left( \frac{|\iint E_{wg} E_{fb} \, dx \, dy|^2}{\iint |E_{wg}|^2 \, dx \, dy \iint |E_{fb}|^2 \, dx \, dy} \right) \quad (3.6)$$

where  $E_{wg}$  and  $E_{fb}$  are the electric field distribution of the waveguide and fiber modes, respectively. The intensity profiles of both the fiber and the waveguide are acquired with the CCD camera, keeping fixed the distance between the objective and the camera, which in turn keeps fixed the scaling factor. The electric-field distribution  $E(x, y)$  can be retrieved from the intensity profile of the mode for single mode waveguides. Indeed, since the fundamental mode does not have sign inversions, the electric field distribution in the  $xy$  plane (that contains the waveguide cross-section) is given by:

$$E(x, y) = C \sqrt{I(x, y)} \quad (3.7)$$

where  $I(x, y)$  is the measurement intensity profile and  $C$  is a real-valued constant. The overlap integral between the two modes is performed numerically using a MATLAB script.

- *Propagation Losses* (PL), are losses due to straight propagation in the waveguide per unit length. These are defined as:

$$PL|_{\text{dB/cm}} = -\frac{10}{L} \log_{10} \left( \frac{P_l}{P_0} \right) \quad (3.8)$$

where  $L$  is the length of the straight waveguide, while  $P(0)$  and  $P(L)$  are the power at the input and output of the waveguide. Direct characterization of propagation losses involves measuring the output power for many different waveguides lengths, upon cutting the sample several times. Such procedure is not always feasible, because it is destructive and time consuming. Alternatively, one can retrieve the propagation losses indirectly as:

$$PL|_{\text{dB/cm}} = \frac{IL|_{\text{dB}} - CL|_{\text{dB}} - FL|_{\text{dB}}}{L_s} \quad (3.9)$$

where  $L_s$  is the waveguide length.

- *Bending Losses* (BL), are the loss terms due to the distortion of the guided mode in a curving waveguide. A theoretical model [61], justifies an exponential behaviour of the bending loss term with respect to the radius of curvature of the waveguides. For circular-bendings:

$$BL|_{\text{dB/cm}} = C_1 e^{-C_2 R} \quad (3.10)$$

where  $C_1, C_2$  are parameters that depends on the properties of the waveguides

and  $R$  is the radius of curvature. Bending losses can be computed comparing the measured losses of straight waveguides and bent waveguides of the same length:

$$BL|_{\text{dB/cm}} = \frac{1}{L_c} [IL|_{\text{dB,BWG}} - IL|_{\text{dB,SWG}}]. \quad (3.11)$$

where  $L_c$  is the length of the curving path,  $P_{out,SWG}$  and  $P_{out,BWG}$  are the power measured at the output of the straight waveguide and the bent waveguide, respectively.

## Chapter 4

# Optimization of waveguide components

Quality of the basic optical components is of fundamental importance to ensure optimal performances of our integrated multiport interferometer. In this Chapter we present the experimental optimization process of waveguides and directional couplers, aimed at achieving low optical losses and high reproducibility.

### 4.1 Waveguide optimization

In femtosecond laser inscription processes, various parameters need to be optimized depending on the particular application or substrate.

The integrated interferometer is meant to work with quantum dot single-photon sources, emitting at 925 nm. Therefore, we need to optimize single-mode waveguides at this wavelength. In particular, we need good matching with external optical fibers and low losses figures. Indeed, optical losses affect the measurement time, especially in multi-photon coincidence experiments.

Since the number of inscription parameters is very large, we only focused on two variables that are easy to control and proven very effective in the literature: the number of scans and the beam irradiation power. Other process specifications were referred to literature or previous experience of the research group with the same substrate and wavelength.

Waveguide fabrication was performed with the setup described in Section 3.1. The laser repetition rate was set to 1 MHz and pulse duration to 170 fs. Waveguides were inscribed in 1.1 mm thick alumino-borosilicate glass samples (EagleXG, Corning).

Moreover, all waveguides were fabricated 35  $\mu\text{m}$  below the sample surface. This choice increases the efficiency of the thermal phase-shifters: indeed, to achieve an effective modulation of the refractive index and keep a low power dissipation, waveguides must be placed near the surface.

Laser irradiation was performed with multi-pass technique, which allows to achieve waveguides with a higher index contrast by exploiting several superimposed laser scans. Furthermore, this technique improves the confinement properties of the waveg-

uide which is useful for obtaining small bending radii and more compact devices [46].

#### 4.1.1 Optimization of propagation and coupling losses

Waveguides were fabricated with either 3 or 6 overlapped scans, exploring a wide range of values for the irradiation power, from 260 mW to 540 mW. The samples were characterized using a laser diode at 904nm and the apparatus of Section 3.3.2.

Mode acquisition allowed to evaluate the overlap integral between the mode of the single-mode fiber (780HP, ThorLabs) and the inscribed waveguides, leading to the estimation of the coupling losses. All the waveguides written above 390 mW consistently showed either multiple guiding regions or supported multiple modes, being therefore unsuitable for our purposes, whereas single-mode behaviour was observed for lower power.

We measured insertion losses for all the waveguides and, using the methods introduced in Section 3.3.4, we also separate the different loss terms (see Figure 4.1 a). Coupling losses and propagation losses are shown in detail in panel b) and c) of Figure 4.1.

We note that both the coupling losses and propagation losses are lower in the case of 6 scans throughout the whole range of irradiation power. In fact, the insertion losses are consistently lower for these waveguides with respect to the one fabricated with 3 scans.

Besides, waveguides written with irradiation power above 320 mW shows comparable values of coupling losses while propagation losses have a minimum in the interval 310 mW ÷ 340 mW.

We chose as the optimal waveguide, the one fabricated at 320 mW as it has the lowest value of propagation losses (0.18 dB/cm), while having low coupling losses at 0.32 dB. In fact, this waveguide also has the lower insertion losses among the waveguides in the set.

The optimal parameters, adopted from now on through this work, are reported in Table 4.1.

<b>Fabrication parameters</b>	
Substrate	EagleXG
Laser system	PHAROS
Repetition rate	1 MHz
Pulse duration	170 fs
Power	320 mW
Fabrication depth	35 $\mu\text{m}$
Writing speed	20 mm s <sup>-1</sup>
Number of scans	6

**Table 4.1:** Optimal inscription parameters for single-mode waveguides at 925 nm.

## 4.1 Waveguide optimization

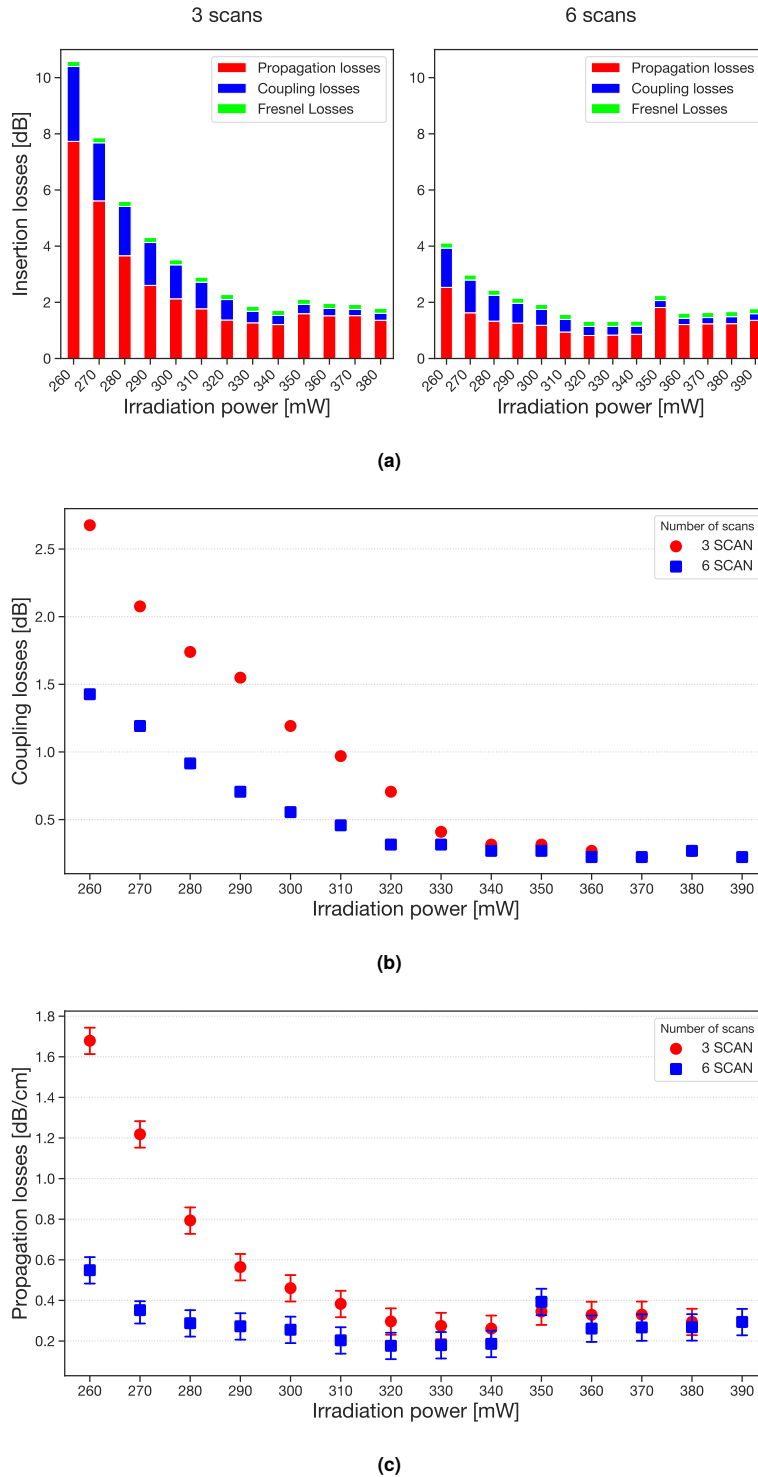


**Figure 4.1:** **a)** Insertion loss figures for femtosecond laser written waveguides with 3 and 6 scans (left and right panel respectively). For each straight waveguide, the three loss contributions have been highlighted (see Section 3.3.4). **b)** Coupling losses **c)** Propagation losses for the 3 and 6 scans waveguides as a function of the irradiation power of the laser beam.

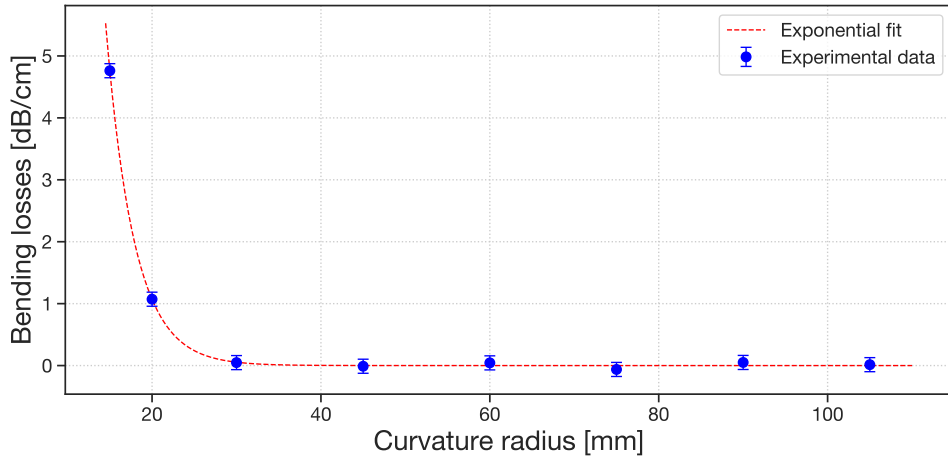


**Figure 4.2:** Bending losses for S-bends with curvature radii ranging in 105 mm–15 mm. The continuous line is the best-fit exponential function.

#### 4.1.2 Characterization of bending losses

Since the footprint of the final device is constrained by the minimum curvature radius achievable without significant losses, an assessment of the bending losses of the waveguides is necessary.

Bending losses are radiation losses due to curvature of the guiding path along the propagating direction. In the curved section, the electric-field mode profile of a single mode fiber is deformed and the field is pushed towards the outer region. As a consequence, there is an increase in coupling with the cladding modes and light is radiated away from the core region. For circular bends, these losses increase exponentially as the radius decreases (as in (3.10)).

We proceeded with the fabrication of S-bends (i.e., two subsequent circular arcs forming a S-shaped waveguide) with bending radii ranging from 105 mm to 15 mm, taking care of keeping the same total curved length for each waveguide. Straight waveguides were fabricated as well, allowing to measure the propagation losses on the straight segment and retrieve the bending losses by means of Eq. (3.11)

Measured bending losses were negligible for curvature radii above 45 mm (see Figure 4.2).

## 4.2 Directional couplers optimization

Another fundamental step for the design and implementation of our integrated interferometer is the optimization of the directional couplers. In order to do so we present a brief theoretical inset on coupled mode theory for directional couplers and discuss the experimental results.

### 4.2.1 Coupled mode theory and best-fit

Under the assumption of weakly coupling between waveguides, in which the guiding regions are not too close to one another, the modes of directional coupler can be considered as a linear combination of the modes of two separated waveguides each of them guiding a single mode. The overall field distribution in the structure is given by:

$$E = A_1(z)E_1(x, y)e^{-i\beta_1 z} + A_2(z)E_2(x, y)e^{-i\beta_2 z} \quad (4.1)$$

where  $\beta_i$  is the propagation constant in the  $i$ -th waveguide, and the field distribution in the individual waveguide is factorized in two contribution:  $A_i(z)$  and  $E_i(x, y)$ .  $A_i(z)$  is the amplitude term that depends on the propagation coordinate  $z$ , while  $E_i$  is the field distribution in the fundamental mode of the  $i$ -th waveguide (which is independent of the direction of propagation).

One can study the evolution of  $A_1(z)$  and  $A_2(z)$  using the coupled-mode equations [62]:

$$\begin{cases} \frac{dA_1}{dz} = -ik_{11}A_1 - ik_{12}A_2e^{j\Delta\beta z} \\ \frac{dA_2}{dz} = -ik_{21}A_1e^{-j\Delta\beta z} - ik_{22}A_2 \end{cases} \quad (4.2)$$

where  $\Delta\beta$  is defined as  $\Delta\beta = \beta_1 - \beta_2$  and the  $k_{ij}$  is the coupling coefficient. The latter is defined by means of the following overlap integral:

$$k_{ij} = \frac{k_0 \iint E_i^* \Delta n_j(x, y)^2 E_j dx dy}{2n_i \iint E_i^* E_j dx dy} \quad (4.3)$$

where  $\Delta n_j$  is the difference between the refractive index of waveguide  $j$  and the refractive index in the generic point  $(x, y)$  as:

$$\Delta n_j(x, y) = n_j - n(x, y). \quad (4.4)$$

Assuming that the index profile of the two waveguides is identical, which is a reasonable assumption for our femtosecond laser written waveguides, we retrieve  $\Delta\beta = 0$ ,  $k_{ij} = k_{ji} = k$  and  $k_{ii} = k_{jj} = 0$ , and thus (4.2) is simplified as:

$$\begin{cases} \frac{dA_1}{dz} = -ikA_2 \\ \frac{dA_2}{dz} = -ikA_1 \end{cases} \quad (4.5)$$

Defining the vector  $\mathbf{A}(z) = [A_1(z), A_2(z)]$  allows to write the former equation in a more compact form:

$$\frac{d\mathbf{A}}{dz} = -iM(z)\mathbf{A} \quad (4.6)$$

where

$$M(z) = \begin{bmatrix} 0 & k(z) \\ k(z) & 0 \end{bmatrix}. \quad (4.7)$$

We highlighted the  $z$ -dependence of the coupling constant since it depends on the reciprocal distance between the waveguides over the whole length of the structure. The power distribution at a given  $z$ -coordinate, which is given by  $P_i(z) \propto |A_i(z)|^2$ . The  $A_i(z)$  are given by the solution of (4.6) that can be computed using the formula for first order linear differential equations [63]:

$$\mathbf{A}(z) = \mathbf{A}(z_0) e^{-i \int_{z_0}^z M(s) ds} \quad (4.8)$$

We note that we can have evanescent coupling also in the bent segments in which the waveguides come closer to each other. The overall dependence of the reflectivity has a dependence on the coupling length  $L$  as:

$$R = \cos^2(kL - \Phi_0) \quad (4.9)$$

where  $k$  is the coupling constant and  $\Phi_0$  is a term that takes into account this additional coupling effect.

Moreover, the coupling constant  $k(z)$ , decays exponentially with the coupling distance  $d$ , since it depends on the overlap integral of the exponential tails of the fundamental modes of the separate waveguides [64]:

$$k = \alpha e^{-\gamma d(z)} \quad (4.10)$$

where  $\alpha$  and  $\gamma$  are positive parameters,  $d(z)$  is the mutual distance between the waveguides as a function of the propagation coordinate  $z$ , and it takes into account the geometry of the directional coupler.

#### 4.2.2 Preliminary assessment of waveguide quality

For the realization of directional couplers, the waveguides have to be identical. Moreover, if we want to realize several directional coupler in a single device we need waveguides that are reproducible.

The free parameters one can optimize to reach the desired splitting ratios are the coupling length  $L$  and the coupling distance  $d$  as defined in Section 2.3.1. The bending radius used for the directional couplers follows the results of the characterization of the bending losses (see Section 4.1.2). Larger bending radii make the footprint of the final device bigger, leading to an increase of losses due to the longer propagation. On the other hand, using smaller radii leads to significant bending losses and may increase the total losses as well. To face this trade-off, directional couplers were implemented using circular arcs and bending radius of 45 mm and 60 mm.

As a first test, we fabricated a series of directional couplers with fixed coupling distance and a coupling length that varies between  $0 \div 3.5 \mu\text{m}$ , for both radii of curvature.

We computed the experimental reflectivity of the directional couplers as:

$$R_{exp} = \frac{P_{1,out}}{P_{1,out} + P_{2,out}} \quad (4.11)$$

where  $P_{i,out}$  is the measured power at the  $i$ -th output.

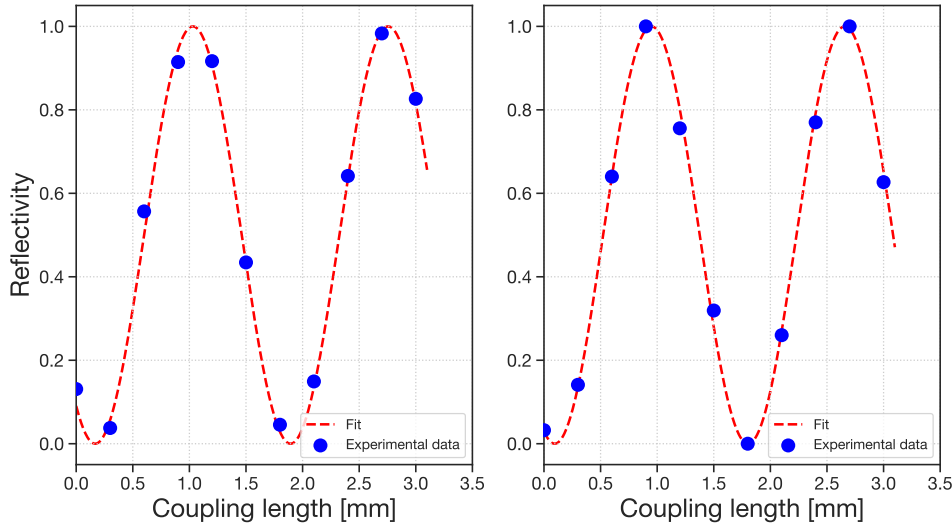


**Figure 4.3:** Reflectivity values as a function of the coupling length  $L$ , for directional couplers fabricated with 45 mm (left panel) and 60 mm (right panel) bending radii. The continuous line is the best-fit sinusoidal function.

We observed a good agreement between the measurements and the theoretical model (see Figure 4.3) which testifies the quality of the waveguides and the stability of the directional couplers. Moreover, the measured reflectivity values cover the whole  $0 \div 1$  range and this is possible only with identical waveguides. This means that the waveguide chosen in Section 4.1.1 is suitable for the realization of directional couplers and therefore we can proceed with the optimization.

### 4.2.3 Coupling distance optimization

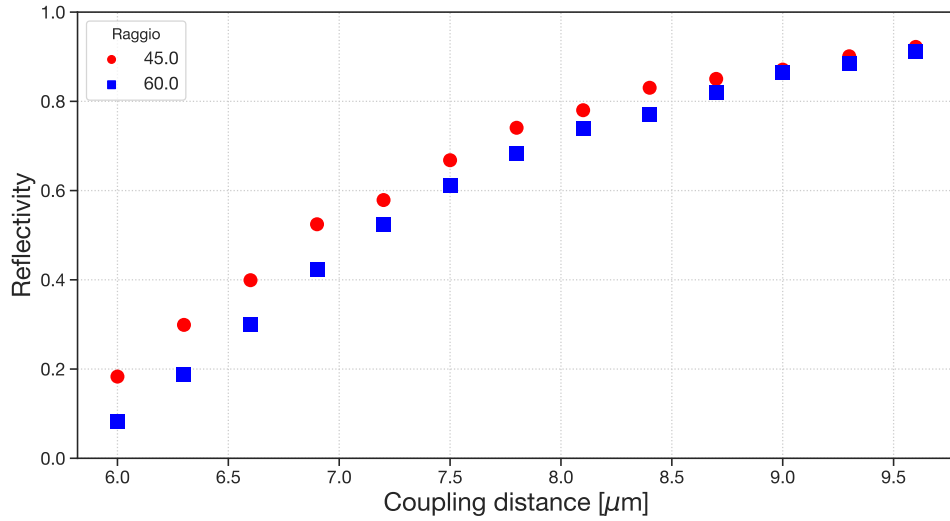
Since we aim for minimization of the overall footprint of the device, we decided to fabricate directional couplers with  $L = 0$  and optimize the coupling distance  $d$  instead. The main drawback of this approach is that the coupling constant  $k$  has an exponential relation with the coupling distance (as in Eq. (4.10)). As a result,  $k$  is very sensitive to the inherent variability of the fabrication process.

We fabricated 13 directional coupler for both radii of curvature  $R = 45$  mm and  $R = 60$  mm. The coupling length is null while the coupling distance  $d$  varies from  $6.0 \mu\text{m}$  to  $9.6 \mu\text{m}$ . The experimental results are reported in Figure 4.4.

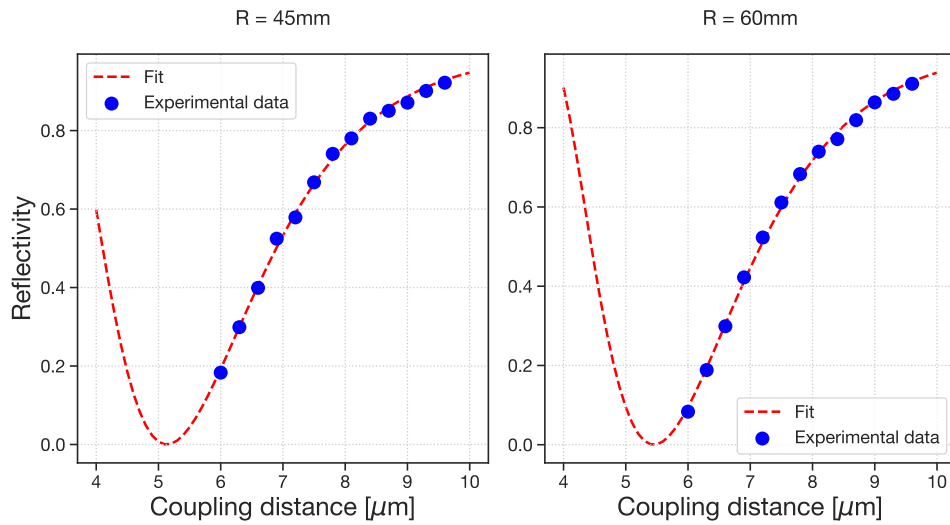
We notice that the balanced directional coupler, for this particular fabrication, has  $d \approx 6.9 \mu\text{m}$  for  $R=45$  mm, while  $d \approx 7.2 \mu\text{m}$  for  $R=60$  mm. Besides, the measurements did not highlight any significant difference in the insertion losses between the devices fabricated with the two different radii.

In order to understand the variability of the coupling coefficient  $k$ , we fabricated several runs of directional couplers and fit the measured values of the reflectivities with a curve  $R_{\alpha,\gamma}(d)$  derived by means of Eq. (4.8) where  $k(z)$  was expressed as in (4.10) with  $\alpha$  and  $\gamma$  as fitting parameters.

We notice a stable value of  $\alpha$  throughout all fabrications for both  $R = 45$  mm and



(a)



(b)

**Figure 4.4:** **a)** Experimental measurements of the directional coupler reflectivity as a function of the coupling distance  $d$ . **b)** Backward simulations of the data for the two radii of curvature,  $R = 45$  mm (left panel) and  $R = 60$  mm (right panel). The figure shows the how the reflectivity evolves in the case of  $L = 0$ . We fit the reflectivity values with a simulation based on the coupled equation in the waveguide coupling theory. It was assumed that the coupling coefficient depends exponentially on the coupling distance as in (4.10).

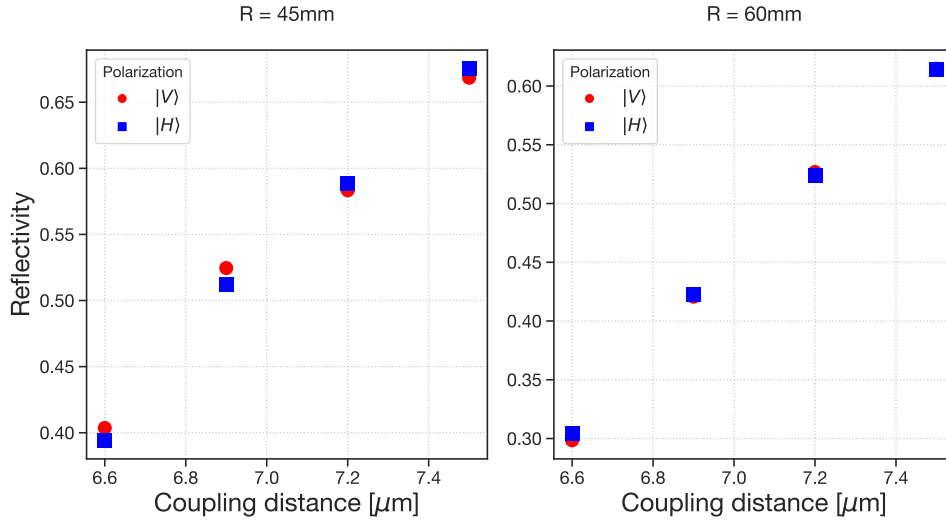


**Figure 4.5:** Reflectivity of the directional couplers at 45 mm (left panel) and 60 mm (right panel) measured with horizontally and vertically polarized light.

$R = 60$  mm. On the other hand we note variations of about 10 % for the exponential decay constant  $\gamma$ . This coefficient is more relevant, as it is the driving force for the splitting ratio in the directional couplers and the main indicator of the fabrication variability. From our fabrications, the average value of the decay constant is  $\langle \gamma \rangle = 105.73 \pm 8.62 \text{ mm}^{-1}$  for  $R = 45$  mm and  $\langle \gamma \rangle = 118.54 \pm 13.68 \text{ mm}^{-1}$  for  $R = 60$  mm. We used these information for fine-tune the fabrication interval for  $d$  in order to make it robust to the experimental variability and also to be sure it contains the balanced directional coupler.

#### 4.2.4 Polarization sensitivity

As a further analysis, we measured the splitting ratios of the couplers, for distances  $d$  in the neighbourhood of the 50:50 transmissivity, for both H- and V-polarized light. To this purpose we adopted the end-fire setup discussed in Section 3.3.2, modified by adding a  $\lambda/2$  and a  $\lambda/4$  waveplates are inserted, before the fiber. However, the optical fiber introduces a polarization rotation that cannot be easily predicted since it depends on the twists and windings of the fiber itself. The waveplates were empirically set in such a way to introduce a polarization rotation that, combined with the inherent rotation of the fiber, leads to a H and V polarization states at the input of the integrated device.

The measured reflectivities for both polarizations are reported in Figure 4.5. The directional couplers show good polarization independence with differences in splitting ratio (between H and V input light) that is less than 1%. This result is in agreement with Ref. [52].



## Chapter 5

# Fabrication of passive interferometric circuit

In Section 1.5 we showed how to assess the genuine indistinguishability of  $n$ -photons by means of a specific multiport interferometer. In the following Chapter we present the optimization steps for the design of the layout, the fabrication and the characterization of an integrated-optics circuit implementing that scheme, which can be used to evaluate the indistinguishability of 4 photons.

### 5.1 Circuit geometry design

The aim of the experimental work of this Thesis is the realization of a  $n = 4$  version of the circuit proposed in Section 1.5.

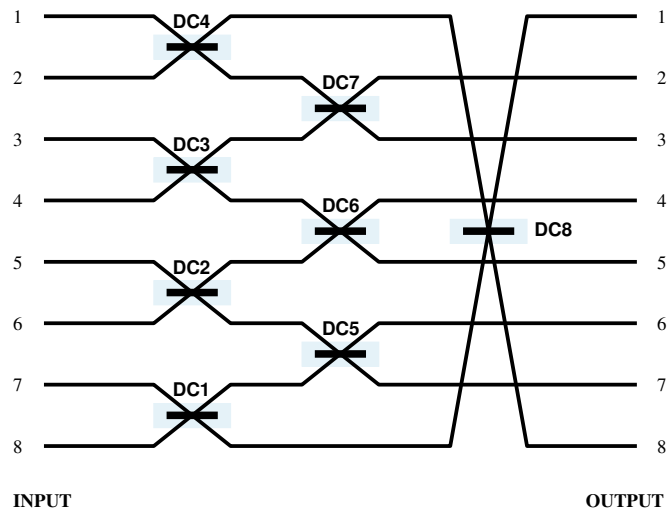
The design of the integrated circuit has been optimized considering the geometrical constraints of the optical components and with the aim of minimizing losses and achieving stable and identical directional couplers.

The transition from the 8-modes theoretical scheme to the integrated photonic device is straightforward by replacing each beam-splitter with a directional coupler (see Figure 5.1).

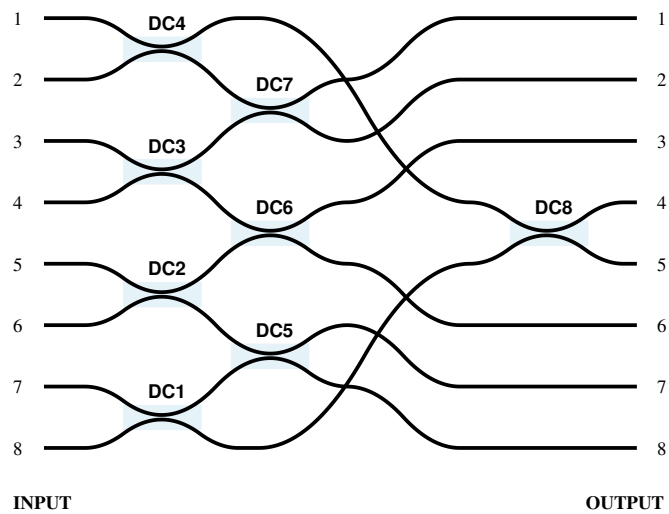
Given the number of curved waveguides segments and directional couplers in the device, we chose to set the minimum radius of curvature to 60 mm. In fact, by keeping some margin with respect to the minimum bending radius pointed out in the preliminary characterization (Section 4.1.2), we are less sensitive to the losses that several consecutive curves may introduce, while keeping a compact footprint.

In addition, adjacent optical modes at the input and output facets have to be fabricated with a pitch equal to the one of the fiber arrays, namely 127  $\mu\text{m}$ .

It is apparent from Figure 5.1b that, in order to bring the outer mode together to the directional coupler DC8, it is necessary to realize a “crossing” between the waveguides. Clearly, it cannot be done while keeping all the optical channels at the same depth, since intersections may introduce undesired coupling between the modes and additional losses. However, we can exploit the 3D capabilities of the femtosecond laser micromachining technology to create bridge-like structure.



(a)



(b)

**Figure 5.1:** a) Scheme of the interferometer for the 4-photons experiment. b) Top-view of the integrated optical design of the circuit. The transition between the two is given by substituting each beam-splitter in a) with a balanced directional coupler. Moreover, after the coupler, the external modes are kept in the middle of the device to allow a more compact footprint. The figures are not in scale.

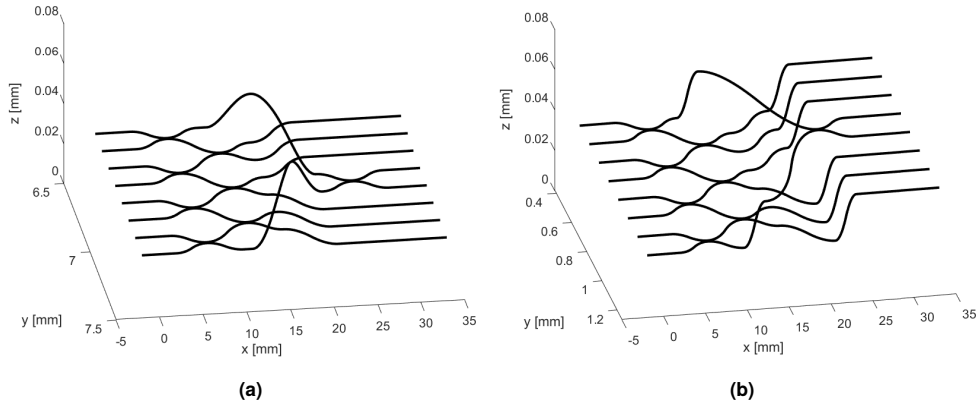


**Figure 5.2:** Schemes of the two proposed layouts. **a)** Co-planar layout. **b)** Dual-planar layout. The axis are not in scale.

On the other hand, even this solution can introduce some complications. In fact, if the “bridge” section overpasses too closely another optical mode, we can have light exchange between them by means of the evanescent coupling mechanism. In order to assess this issue, we defined a minimum distance of  $25\ \mu\text{m}$  between an optical mode that remains at fixed depth and the optical mode of the bridge. We note that this “crossing height” is much larger than the minimum coupling distance between the two waveguides of a directional coupler, preventing the risks of coupling.

We considered two solutions for the realization of the device:

- *Co-planar layout:* after the first row of directional couplers, the external modes are brought side by side by passing over all the others. Except for the “crossing” segments, connecting DC1 and DC4 with DC8, all waveguides stays at a fixed depth of  $35\ \mu\text{m}$  below the surface (see Figure 5.2a).

The advantage of this configuration is that all directional couplers are placed at the same depth; this improves the stability and reproducibility of the splitting ratios.

- *Dual-planar layout:* after the first row of directional couplers, the external modes are brought  $25\ \mu\text{m}$  deeper (i.e. at  $60\ \mu\text{m}$  depth) and then are brought close together to form the directional coupler DC8. The other modes are connected forming the second row of directional couplers and then are also brought to  $60\ \mu\text{m}$  depth (see Figure 5.2b).

This layout is more compact with respect to the other one (about 10% smaller). On the other hand, it has the drawback that some waveguides portions and the directional coupler DC8 (see Figure 5.1) are fabricated  $60\ \mu\text{m}$  below the surface, which is a different depth than the one waveguides were designed for. This may introduce additional losses and affect the value of the splitting ratio of the out-of-plane directional coupler.

The schemes of Figure 5.2 were realized with a point-to-point representation using a custom MATLAB script that generates the entire series of points that controls the motions stages during the fabrication.

The out-of-plane bend segments of both layouts were realized with a sine-squared function that provides smooth transitions while being easy to control and adjust to suit the “crossing height” parameter.

We also monitored some other parameters regarding geometrical constraints and the limitations of the motion stages when designing the layouts for the integrated circuit. In particular:

- The *number of points per second*. Indeed the motion stages drivers can manage a finite number of instructions (or points) per second. Since the translation velocity was determined in Section 4.1 to 20 mm/s, we had to find the proper points-per-second density that allows accurate representation of the curved segments without saturating the motion stages capabilities.  
In order to do so, we fabricated six directional couplers of three different types with coupling distance ranging from 6.6  $\mu\text{m}$  to 7.5  $\mu\text{m}$  for a total of 18 devices. A first type in which the curves were realized with native G-Code circular arcs and the other two were realized with point-to-point representation using two commands-per-second (cmd/s) values: 200 cmd/s and 400 cmd/s. We characterized the directional coupler to assess differences in insertion losses between the three types. The three kind of devices were completely equivalent, and therefore we opted to use 200 cmd/s being the less demanding value for the motion stages while having the same performances of the higher 400 cmd/s.
- The *three dimensional curvature* of the optical modes. In order to ensure a maximum curvature radius for the crossing segments that is higher than the limit of 60 mm, we implemented, in the same script that generates the list of points for the motion stages, a check for the three dimensional curvature. This has been used to properly model and size the out-of-plane bend segments.

In order to choose the optimal layout, we fabricated ten interferometers: five devices with the co-planar layout and five with the dual-planar layout. The values of the coupling distances for the directional couplers were identical among the two types of devices, ranging from 6.2  $\mu\text{m}$  to 7.4  $\mu\text{m}$ .

Insertion losses were characterized by coupling a single input of each the devices with light at 904 nm. Unlike straight waveguides, the input power is distributed in four different output modes. Therefore, we can define the insertion losses for a single channel as:

$$IL|_{\text{dB},mode} = 10 \log_{10} \left( \frac{P_{in}}{\sum_i P_{out,i}} \right) \quad (5.1)$$

where the summation runs over all the output modes.

The two kind of devices showed comparable losses, namely  $IL_{co} = 1.71 \pm 0.13$  dB for the co-planar, and  $IL_{dual} = 1.79 \pm 0.09$  dB for the dual-planar layout.

Furthermore, we are interested in having a device with uniform losses among all the optical modes. Therefore, we chose a single device for each layout and measured the insertion losses for each input mode with horizontally and vertically polarized light at 904 nm.

While the differences between the losses for H- and V-polarized light were negligible for both devices, we found an average insertion loss among the input modes of the co-planar layout to be  $IL_{co} = 1.36 \pm 0.12$  dB and  $IL_{dual} = 1.67 \pm 1.01$  dB for the dual-planar layout.

Despite the difference in footprints, the overall losses the two device are very similar but we note a higher variability among the different modes for the second design. Therefore, we decided to adopt the co-planar layout.

## 5.2 Device fabrication of the device

### 5.2.1 Fabrication and preliminary characterization

After the choice of the design of the integrated circuit layout, we proceeded with the fabrication of eleven devices with coupling distance ranging from  $6.7 \mu\text{m}$  to  $7.7 \mu\text{m}$ . The other geometrical parameters of the devices are reported in Table 5.1.

Geometrical parameters	
Width	0.889 mm
Length	29.65 mm
Modes pitch	127.0 $\mu\text{m}$
Maximum crossing height	25.0 $\mu\text{m}$
Minimum curvature radius	60.0 mm

**Table 5.1:** Geometrical parameters of the multipoint integrated interferometers.

A preliminary characterization of the reflectivity of the devices was carried out using the manual manipulator setup presented in Section 3.3.2 at two different wavelength: 904 nm and 940 nm. This allows to make prediction on the actual reflectivity of the interferometers in the neighbour of 925 nm by means of a linear interpolation.

The reflectivity values for both wavelength as well as the interpolation at 925 nm are reported in Table 5.2 where the devices whose directional couplers have reflectivity values closer to 50 % are highlighted.

We chose these two devices for a more thorough characterization using the hexapod setup (see Section 3.3.2). This setup allows for a more precise and stable control of the fiber-waveguide coupling and it is equipped with a laser diode emitting at 925 nm which is a wavelength closer to the one of the quantum dot sources of the experiment. Moreover, the characterization was carried out using vertically and horizontally polarized light.

### 5.2.2 Insertion losses characterization at 925 nm

The characterization of losses for each mode is performed by coupling light in every input mode of the devices. On the same sample, we also fabricated straight waveguides which are used as reference. Insertion losses figures for each mode are reported in Figure 5.3.

<b>Reflectivity values</b>				
Device number	Coupling distance [ $\mu\text{m}$ ]	Reflectivity values [%]		
		904 nm	925 nm	940 nm
1	6.7	50.8	45.8	42.2
2	6.8	53.2	47.8	43.9
3	6.9	55.0	50.3	47.0
4	7.0	58.7	54.2	50.9
5	7.1	60.0	54.4	50.4
6	7.2	65.5	61.1	57.9
7	7.3	66.5	62.0	58.7
8	7.4	68.2	63.8	60.7
9	7.5	73.3	69.3	66.5
10	7.6	73.6	69.6	66.8
11	7.7	77.7	73.8	71.1

**Table 5.2:** Reflectivity values for all the multiport interferometers measured at 904 nm and 940 nm. Interpolated values at 925 nm are reported as well.

We measured insertion losses averaged over all modes for both the horizontally and vertically polarized light recovering values of  $IL_H = 1.20 \pm 0.02$  dB and  $IL_V = 1.17 \pm 0.03$  dB for the device with coupling distance  $d_c = 6.8 \mu\text{m}$  while for the device with  $d_c = 6.9 \mu\text{m}$  we retrieved  $IL_H = 1.15 \pm 0.05$  dB and  $IL_V = 1.11 \pm 0.03$  dB.

We note that these values are remarkably close to value measured for the straight waveguide,  $IL_{SWG} = 1.108$  dB. This is consistent with the characterization of the bending losses for curvature radii of  $R = 60$  mm. Moreover, the average insertion losses for the horizontally and vertically polarized light are equivalent, highlighting good independence on the input polarization state.

### 5.2.3 Splitting ratio characterization at 925 nm

The characterization of the splitting ratios of the eight directional couplers is carried out with a procedure similar to the one used in Section 4.2.2. In this case, however, we had to characterize a network made of two cascaded rows of directional couplers. Considering the situation of Figure 5.4, the reflectivity of the directional couplers belonging to the second row can be retrieved directly from the measurements of the output powers, and by injecting light only in input  $IN_1$ . In detail:

$$\begin{cases} R_1 = \frac{P_{OUT_{12}}}{P_{OUT_{11}} + P_{OUT_{12}}} \\ R_2 = \frac{P_{OUT_{21}}}{P_{OUT_{21}} + P_{OUT_{22}}} \end{cases} \quad (5.2)$$

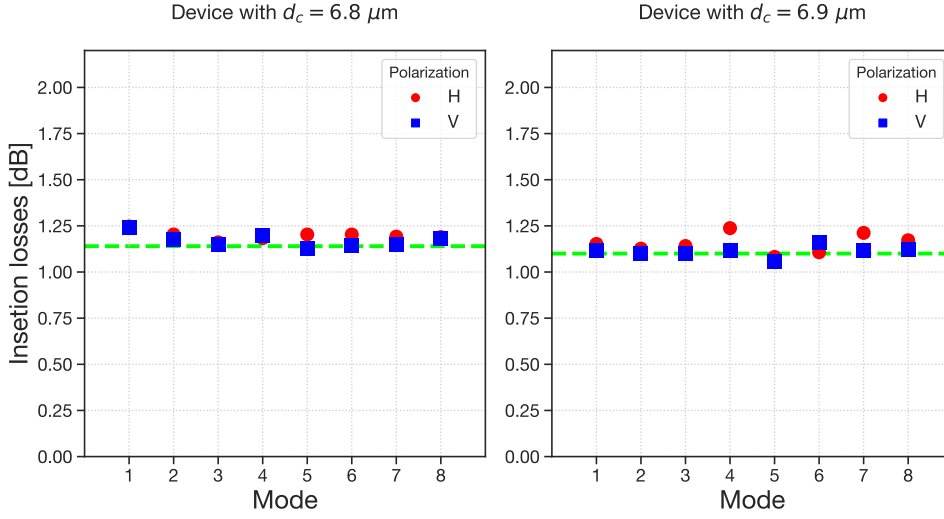


**Figure 5.3:** Single-mode insertion losses for horizontally and vertically polarized light measured for the device with coupling length  $d_c = 6.8 \mu\text{m}$  (left panel) and  $d_c = 6.9 \mu\text{m}$  (right panel). The dashed line is plotted as reference and represents the insertion loss of the straight waveguide.

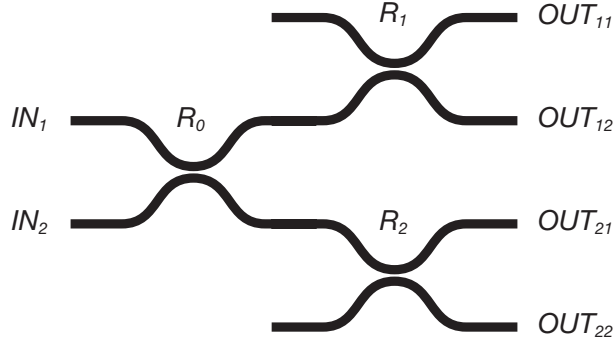


**Figure 5.4:** Schematic representation of a two rows cascading directional couplers.

We could also retrieve  $R_0$  by calculating:

$$R_0 = \frac{P_{OUT_{11}} + P_{OUT_{12}}}{\sum_i P_{OUT_{1i}} + \sum_i P_{OUT_{2i}}}. \quad (5.3)$$

Actually, estimation of  $R_0$  by Eq. (5.3) turn out to be less accurate that the estimation of  $R_1$  and  $R_2$  using Eq. (5.2). In fact, after the first coupler, the light propagates along different paths and Eq. (5.3) is very sensitive to differential losses between them. This may be particularly true for the external directional couplers (namely, DC1 and DC4 in Figure 5.1) due to the presence of the “bridge” section. Indeed, the out-of-plane waveguide segments may introduce additional losses with respect to the other ones that remain in the same plane.

Therefore, we adopted a more precise and robust calculation that exploits the information of two different measurements, by injecting light in two input modes. To this

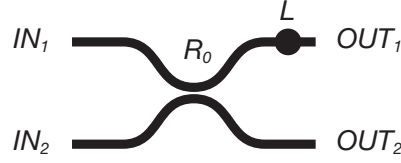


**Figure 5.5:** Schematic representation of a directional coupler with a differential loss  $L$  between the output modes.

purpose, we can examine the situation represented in Figure 5.5 where we consider a directional coupler with reflectivity  $R_0$  with a differential loss  $L$  in one of the two output modes.

Injecting light in both  $IN_1$  and  $IN_2$  we can write the following system of equations:

$$\begin{cases} P_{11} = P_1 \cdot R_0 L \\ P_{21} = P_1 \cdot (1 - R_0) \\ P_{12} = P_2 \cdot (1 - R_0) L \\ P_{22} = P_2 \cdot R_0 \end{cases} \quad (5.4)$$

where  $P_{ij}$  is the output power in mode  $i$  when power  $P_j$  is injected in mode  $j$ . We can define the auxiliary variable  $C$  as:

$$C = \sqrt{\frac{P_{11} P_{22}}{P_{21} P_{12}}}. \quad (5.5)$$

We note that:

$$C = \sqrt{\frac{P_{11} P_{22}}{P_{21} P_{12}}} = \sqrt{\frac{R_0^2 L}{(1 - R_0)^2 L}} = \frac{R_0}{1 - R_0}. \quad (5.6)$$

Therefore, it is not difficult to show that the values of  $R_0$  and  $L$  can be retrieved as:

$$\begin{cases} R_0 = \frac{C}{C + 1} \\ L = \frac{P_{11}}{P_1} \cdot \left(1 + \frac{1}{C}\right) \end{cases} \quad (5.7)$$

This model allows to retrieve the value of  $R_0$  also in the presence of differential losses in the output modes.

Moreover, it can be used for the retrieval of the reflectivity  $R_0$  in Figure 5.4 where  $OUT_1 = OUT_{11} + OUT_{12}$  and  $OUT_2 = OUT_{21} + OUT_{22}$ . The estimates of the reflectivity values for directional couplers of the first row is independent on  $P_i$  (namely, the amount of coupled light) highlighting the robustness of the model, and we can recover  $R_0$  from the value of  $C$  which only depends on known quantities that are measured during the characterization process.

The values of reflectivity of the eight directional couplers for the devices with  $d_c = 6.8 \mu\text{m}$  and  $d_c = 6.9 \mu\text{m}$  are reported in Table 5.3 and Table 5.4 respectively.

## 5.2 Device fabrication of the device

---

These devices result to be reasonably close to the nominal design parameters and was chosen to undergo further processing steps to make its internal phase reconfigurable.

DC	Reflectivity	Reflectivity
	H-polarization	V-polarization
	[%]	[%]
1	48.3	48.2
2	47.7	47.6
3	45.9	45.9
4	45.4	45.3
5	50.0	49.9
6	49.2	49.0
7	46.8	48.3
8	50.0	49.9

**Table 5.3:** Reflectivity of the directional couplers measured with horizontally and vertically polarized light for the device with coupling distance  $d_c = 6.8 \mu\text{m}$ . The reflectivities measured for H- and V-polarized light, are very similar to each other. In particular, we computed average values of  $R_H = 47.9 \pm 1.7 \%$  and  $R_V = 48.0 \pm 1.6 \%$ .

DC	Reflectivity	Reflectivity
	H-polarization	V-polarization
	[%]	[%]
1	50.5	50.2
2	50.9	50.8
3	50.5	50.5
4	50.7	50.7
5	50.7	50.6
6	51.3	51.1
7	50.4	50.5
8	53.5	53.3

**Table 5.4:** Reflectivity of the directional couplers measured with horizontally and vertically polarized light for the device with coupling distance  $d_c = 6.9 \mu\text{m}$ . The reflectivities measured for H- and V-polarized light, are very similar to each other. In particular, we computed average values of  $R_H = 51.1 \pm 0.9 \%$  and  $R_V = 51.0 \pm 0.9 \%$ .



## Chapter 6

# Fabrication of reconfigurable interferometric circuit

After the fabrication of the optical interferometric circuit, we proceeded with the design and the realization of the thermal-optic phase-shifters to control the internal phase of the interferometer. In this Chapter, we present the design steps of the microheaters, the characterization of the phase shifting operation and the final assembly of the device.

### 6.1 Design of the thermal phase-shifters

An accurate design of the microheaters is needed in order to induce a full  $2\pi$  phase shift with low power dissipation, and ensure stable operation of the interferometer over a long period of time.

The electrical properties of the microheaters are set by their geometrical parameters: considering a rectangular heater, these are the thickness  $h$  of the gold layer, the length  $l$  and the width  $w$ . In particular, the resistance is given by:

$$R = \frac{\rho}{h} \frac{l}{w} \quad (6.1)$$

where  $\rho$  is the electrical resistivity of the gold layer. The thickness of the metallic layer is fixed to  $h = 100$  nm by the deposition process (see Section 3.2.2), therefore the free parameter for the sizing of the total resistance is the aspect ratio  $l/w$ . Following the directions of Ref. [60] we set this parameter to  $l/w = 16.67$  in order to achieve resistances of about  $80 \Omega$ .

Moreover, in order to achieve a durable and stable operation of the microheaters, and avoid ruptures of the gold film, their design operation temperature should be the lowest possible. To this purpose we employed two expedients:

- *Large are of the microheaters.* Indeed, a larger area allows to dissipate the same amount of power with a lower temperature on the heater. Adopting the values  $l = 5$  mm and  $w = 30 \mu\text{m}$  the thermal-shifters that are still compact but with peak temperatures, when operated, that are more relaxed.

- *Improved efficiency by improved isolation.* To minimize the thermal diffusion to other waveguides, and reduce the power needed to achieve a given phase shift, a 50  $\mu\text{m}$ -wide stripes of gold is removed from both sides of each thermal-shifter. Based on previous knowledge of the research group, this procedure allows an isolation improvement of about 15 %.

Summarizing, the final parameters adopted for the geometry of the microheaters are  $l = 5 \text{ mm}$ ,  $w = 30 \mu\text{m}$  and  $h = 100 \text{ nm}$ .

Our interferometer was equipped with three microheaters, as in Figure 6.1. This allowed to have redundant resistances, and therefore to ensure reliable operation of the device even in case of damages or failures of one thermal shifter. Furthermore, the three microheaters can be used together allowing a finer control over the phase modulation.

The microheaters are designed to follow the path of the waveguides. However, given the geometrical constraints and the small size of the integrated device, only the R1 and R3 microheaters are realized with the specifications reported above, while R2 is a back-up heater which is realized with the same width of the other two and a length of 2.5 mm due to space constraints. We expect, for microheaters with this parameters, to have operational limits of dissipated electrical power on a single resistor of 500 mW when driving R1 and R3, while the limit for R2 is 250 mW.

The thermal shifters were patterned on the two devices characterized in Section 5.2: the device with optimal reflectivities and the other, that still possess acceptable reflectivity values, is patterned in order to be used a back-up device in case of damages to the film layer during the ablation process. In the current Chapter we call “Device 1(2)” the device with directional couplers realized with coupling distance  $d_c = 6.8 \mu\text{m}$  ( $d_c = 6.9 \mu\text{m}$ ).

The conductive patterns (see Section 3.2.2) were designed in such a way to minimize the aspect ratio  $l/w$  of the gold tracks before and after the microheaters and using as much metallic surface as possible. In this way, the resistance of these tracks is negligible with respect to the resistance of the microheaters allowing to dissipate power only on the desired regions. The ablation pattern is shown in Figure 6.2, where the black lines represent the portion of gold that is removed by the laser ablation; the difference in size of these gold tracks and the thin gold stripes of the microheaters (left panel) is clearly visible.

The device was mounted on a 8 cm  $\times$  2.9 cm  $\times$  0.5 cm aluminum slab, functioning as heat sink. Thermal contact was ensured by means of a thermally-conductive paste. This paste also ensures the absence of air bubbles between the aluminum base and the glass sample, therefore maximizing the heat transfer.

Two custom connector boards were realized for interfacing the device with standard electrical equipment by means of 2.54 mm pin headers (see left panel of Figure 6.2). Electrical bonding between the gold layer and the boards is realized with electrically-conductive epoxy glue.

The glass sample is fixed to the aluminum base by means of the same conductive paste because, upon drying, it behaves like a glue ensuring a stable hold. In addition, the sample was mechanically clamped between the two electrical boards.

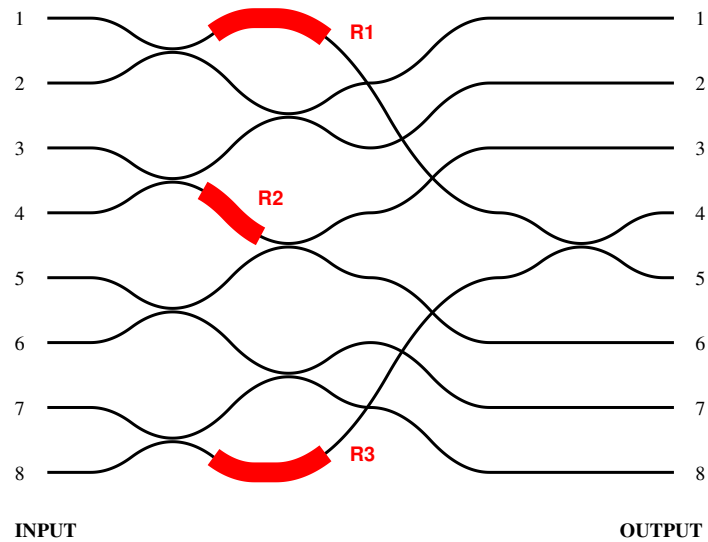


**Figure 6.1:** Schematic top-view of the interferometer. Rx indicate the resistors patterned on the chip surface, which enable thermo-optic control of the phases in the circuit.

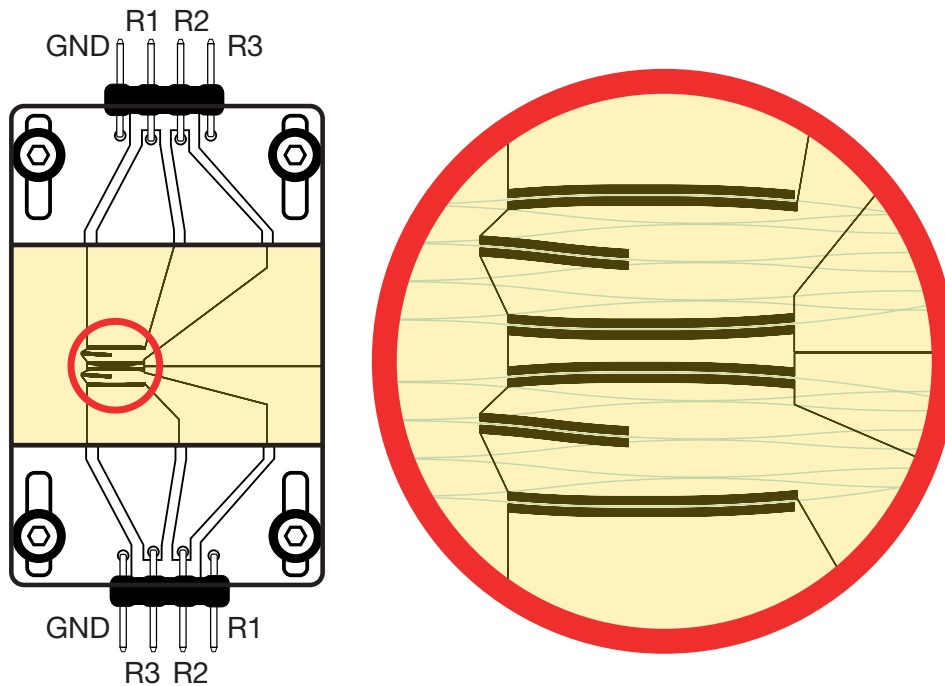


**Figure 6.2:** Scheme of the electrical connections and ablation pattern for the thermal shifters. Resistors are patterned above two adjacent interferometers. The electrical contacts for the resistors R1, R2 and R3 of Figure 6.1 (as well as the common ground (GND)) are indicated near the pin headers. On the right, we report a magnified view of the ablation pattern. One can note the six resistive stripes on top of the waveguides and the portions of gold that is removed on the sides of the microheaters (as dark regions).

We also successfully tested the electrical isolation of the patterned tracks and measured the resistance values of the microheaters at the PoliFAB laboratories. The values of the resistors were measured with 100 mV driving voltage are reported in Table 6.1.

<b>Resistance values</b>		
	phase-shifter	Resistance value [ $\Omega$ ]
Device 1 ( $d_c = 6.8 \mu\text{m}$ )	R1	81.3
	R2	45.6
	R3	83.7
Device 2 ( $d_c = 6.9 \mu\text{m}$ )	R1	82.1
	R2	54.6
	R3	86.8

**Table 6.1:** Thermal shifters resistance measured with a driving voltage of 100 mV.

## 6.2 Characterization of the thermal phase-shifters

After the fabrication of the thermal phase-shifters, we have to make sure that they are able to drive a  $2\pi$  phase shift. Since the thermal phase-shifters on both devices are identical, we characterize the phase shifting operation of the interferometer with superior optical performances (namely, values of reflectivity of the directional couplers closer to 50 %). In this section we present the characterization for a single microheater fabricated on top of Device 2, e.g. R1, but the derivation is valid for all the others.

The microheaters introduce a phase shifts via Joule heating. Since, in standard condition, the thermal conductivity of glass is much higher than the one of air, the heat is dissipated in the glass volume. The refractive index of glass changes linearly with temperature, therefore, through power dissipation, one can introduce an additional phase delay in each waveguide of the device. Considering a thermal phase-shifter  $R_x$  and the  $i$ -th waveguide of the interferometer

$$\Delta\varphi_i = \sigma_i P \tag{6.2}$$

where  $\sigma_i$  is the coefficient of the linear relation between the total phase delay introduced in the waveguide,  $\Delta\varphi$ , and the power  $P$  dissipated in the resistor.

Even when a single microheater is operating, the phases of all the optical modes are modified. Indeed, when heat diffuses in the glass volume, it creates a temperature gradient decreasing radially from the axis of the microheater affecting all the neighboring modes. As shown in Section 1.5, the phase term of interest for the interferometer is a collective term that depends on all modes of the device, which is  $\alpha = \sum_{j=1} (\phi_{2j-1} - \phi_{2j})$ .

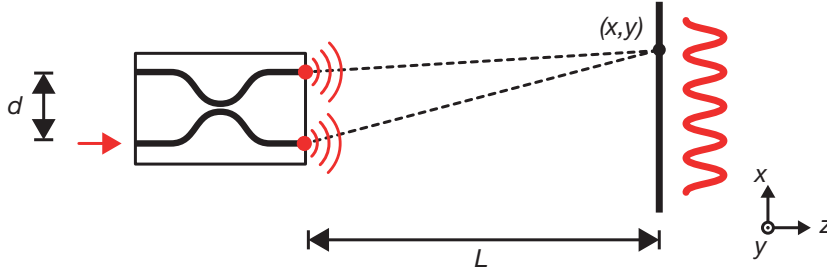


**Figure 6.3:** Scheme of the Young interference experiment. A single input of a balanced directional coupler is coupled, the outputs (which are separated by a distance  $d$ ) behave like two point-like source. In the far-field approximation, the latter give rise to an interference pattern on the image plane at distance  $L$ .

Therefore, using Eq. (6.2), the modulation of the internal phase is given by:

$$\alpha \sim \sum_{j=1}^4 (\sigma_{2j-1} - \sigma_{2j}) P \quad (6.3)$$

$$= (c_{1,2} + c_{3,4} + c_{5,6} + c_{7,8}) P \quad (6.4)$$

where  $c_{i,j} = \sigma_i - \sigma_j$  and  $\sigma_j$  is the coefficient that relates the dissipated power to the phase introduced in waveguide  $j$ . We also note that each  $\sigma_i$  and  $c_{i,j}$  are specific coefficients of each microheater  $R_x$ .

By coupling light in a single input mode, and by observing the output intensity distribution, we are not able to access directly to the value of  $\alpha$ . We recall that the value of  $\alpha$  is visible only when a  $n$ -photons input state is injected into the interferometer. Injecting a coherent light in a single input is equivalent to inject a single photon state, therefore we cannot access the value of  $\alpha$  by monitoring the output intensity distribution. Instead, to estimate  $\alpha$ , we used an indirect technique based on Young interferometry, as we detail in the following.

Let's consider, the system represented in Figure 6.3. Light is coupled into one of the input modes of a balanced directional coupler whose output modes are separated by a distance  $d$ . The output ports act like point-like source and the far-field interference image, generated after a free-space propagation  $L$ , carries information about the phase difference  $\Phi$  between the optical modes:

$$I(x, y) \propto \cos^2 \left( \frac{2\pi d}{\lambda L} x + \Phi \right) \quad (6.5)$$

where  $\lambda$  is the wavelength of the coupled light.

This example can be generalized to suit our purposes. Indeed, the light coupled in a single mode of our integrated interferometer is divided in four output ports. It follows that the interference pattern is more complex, including the spatial frequencies associated to all the different distances between the point-like sources.

By selecting the appropriate spatial frequency term and extracting its phase, we are able to retrieve the phase difference between two modes. Measurements can be performed while driving one microheater with different voltages, therefore, a linear

fit of the dissipated power versus the introduced phase allows to obtain the coefficient  $c_{i,j}$  of Eq. (6.4) associated to the  $i$ -th input mode.

The experimental setup is similar to the one schematized in Figure 6.3. We injected light in input  $i$  of the interferometer and we made light propagate in free-space for a distance  $L$ . The interference pattern is acquired by a CCD camera while varying the power dissipated in a given microheater.

The acquired images were then digitally processed:

- We integrated the intensity map  $I(x, y)$  along the  $y$  coordinate, producing a 1D profile  $I(x)$ , since interference fringes are vertical. This step allows to increase the signal-to-noise ratio of the image;
- The signal  $I(x)$  was processed with a Fast Fourier Transform algorithm;
- We selected the appropriate spatial frequency peak in the spectrum of  $I(x)$  and recorded the phase term of the Fourier transform in correspondence of that peak.

We repeated this procedure for different values of dissipated power and the term  $c_{i,j}$  was computed by fitting a linear model. These steps are represented schematically in Figure 6.4.

Injecting light in all the odd input channels (see Figure 6.1) allows to retrieve experimentally the coefficients  $c_{i,j}$  of Eq. (6.4).

The overall proportional coefficients between  $\alpha$  and the dissipated power,  $C_x$ , for each microheater  $R_x$  is given by the algebraic summation of all the  $c_{i,j}$ . We computed  $C_1 = 29.7 \pm 0.6 \text{ rad W}^{-1}$  and  $C_3 = 29.4 \pm 0.2 \text{ rad W}^{-1}$  respectively for R1 and R3. For the back-up resistor R2 we got  $C_2 = 24.6 \pm 0.2 \text{ rad W}^{-1}$ .

Therefore, considering the power limitations listed above, we estimate that only R1 and R3 are able to drive a  $2\pi$  phase shift by themselves.

### 6.3 Fiber pigtail and packaging

As a final step of the preparation of the integrated interferometer, we proceeded with the fiber pigtailling of the input and output ports using the procedure described in Section 3.2.3.

Moreover, a pair of aluminum wings are screwed to the base for support the delicate fibers of the fiber arrays, further increasing the robustness of the device. The picture of the final device is reported in Figure 6.5.

Input and output modes of the device were aligned with the fiber arrays modes in order to maximize the coupling. After the the gluing procedure, we characterized the insertion losses of the device to check the device performances after the pigtail.

Light was injected into the device input fibers from a fiber-coupled laser by means of standard FC/PC fiber-to-fiber connectors, and we were able to measure input-to-output losses lower than 2 dB. We note that joining fibers together introduce an additional loss term and this may depends even on the connector type. In the final application,

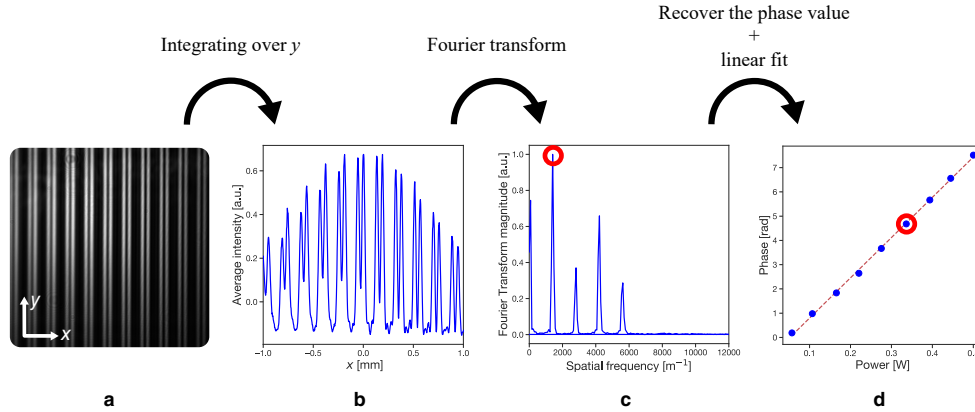


**Figure 6.4:** Power-phase coefficient retrieval procedure. The far-field interference pattern (a) is acquired by the CCD camera. Since the  $y$  direction carries no information on the periodicity of the intensity profile, we integrate  $I(x, y)$  over  $y$  to obtain the signal  $I(x)$  (b). With a Fast Fourier Transform algorithm we compute the spectrum of  $I(x)$  (c). Four peaks are clearly visible, corresponding to four different spatial frequencies. By monitoring the first peak (marked with the red circle) as a function of the dissipated power, we are able to retrieve the proportionality coefficient between the phase shift and the dissipated power (d).

however, the fibers coupled with the single-photon sources will be joined to the fibers of the fiber arrays by means of fiber splicing.

Moreover, we recorded uniform insertion losses among all modes of the interferometer, consistently with the measurements of Section 5.2.2. This confirmed that the fiber arrays were correctly aligned with the input and output modes of the device.

Afterwards, we packed the device and sent it to the CNRS-Center for Nanoscience and Nanotechnology in Paris-Saclay (France), where the quantum experiment will be performed by the group of Prof. Pascale Senellart.

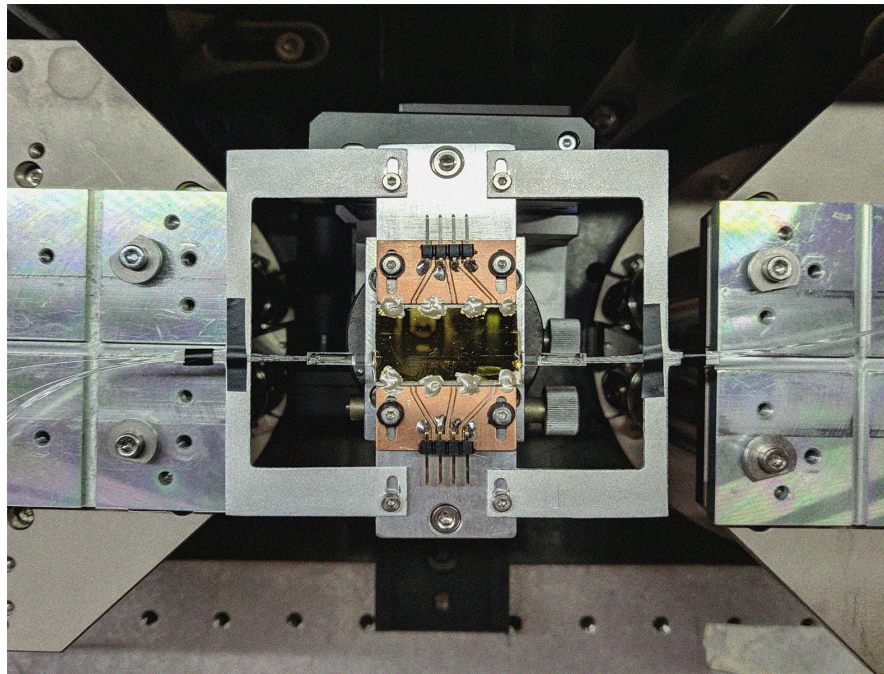


**Figure 6.5:** Picture of the device after the fiber pigtailling procedure.

# Conclusions

In this Thesis work we reported the implementation of an 8-modes reconfigurable interferometer, for the direct characterization of genuine 4-photons indistinguishability. The device was fabricated exploiting the unique three-dimensional capabilities of femtosecond laser micromachining.

To match the emission wavelength of the quantum dot single-photon sources, we developed single-mode optical waveguides in the range 904 nm – 940 nm on aluminoborosilicate glass, yielding propagation losses as low as  $0.18 \text{ dB cm}^{-1}$ . The thermal annealing treatment also allows waveguides to have a good independence on the polarization state of the input light.

The choice of the integrated layout for the interferometer was validated by experimental measurements to minimize overall insertion losses.

Integrated microheaters were patterned on the substrate surface to enable a full  $2\pi$  thermo-optic tuning of the internal phase of the interferometer, with low power dissipation.

Finally, the device was fiber-pigtailed, to enhance the portability and allow easy coupling with external optical fibers. We measured input-output loss figures that were lower than 2 dB.

The interferometer can be used for the qualification of single photon sources, or as a tool for the empirical equalization of the various degrees of freedom of single photons (e.g. temporal delays, polarization state) to be used in quantum information experiments.

Future work can be devoted the fabrication process allowing the fabrication of devices with increased complexity, i.e. higher number of optical modes. Moreover, optical waveguides can be easily re-engineered for different wavelengths, in order to make the device suitable for other single-photon sources such as those based on spontaneous parametric down-conversion.



# Ringraziamenti

Al termine di questo percorso, vorrei innanzitutto ringraziare il professor Roberto Osellame, per avermi accolto nel suo gruppo di ricerca e avermi dato la possibilità di lavorare a questo progetto di tesi.

Un grazie speciale va ad Andrea, per la sua pazienza infinita e per tutte le discussioni (virtuali e non) dalle quali ho imparato molto su come affrontare i problemi e come approcciare la vita in laboratorio.

Voglio ringraziare anche Giacomo, per i suoi tricks da *“buon fabbricatore di guide”* ed per essere stato sempre disponibile ad aiutarmi a risolvere ogni problema.

Un ringraziamento va anche a SimoneP per avermi aiutato a muovere i primi passi in laboratorio, Francesco, SimoneA e tutte le altre persone con cui ho condiviso questi mesi di lavoro.

Ringrazio anche tutti gli amici del Poli, Barbara, Agostino, Amedeo, Felipe, Luca e Votto per tutti i momenti passati assieme in questi cinque anni.

Infine, voglio ringraziare la mia famiglia per l'incoraggiamento e il supporto che mi hanno dato in questi anni.

## *Ringraziamenti*

---

# Bibliography

- [1] S. Marlan O. Scully, Muhammad Suhail Zubairy. *Quantum Optics*. Cambridge University Press (2010).
- [2] L. D. Landau. *Quantum mechanics : non-relativistic theory*. Butterworth Heinemann, Amsterdam (1977).
- [3] A. M. L. Messiah and O. W. Greenberg. *Symmetrization postulate and its experimental foundation*. Physical Review, 136, B248–B267 (1964).
- [4] C. K. Hong et al. *Measurement of subpicosecond time intervals between two photons by interference*. Physical Review Letters, 59, 2044–2046 (1987).
- [5] M. C. Tichy. *Interference of identical particles from entanglement to boson-sampling*. Journal of Physics B: Atomic, Molecular and Optical Physics, 47, 103001 (2014).
- [6] A. Luis and L. L. Sanchez-Soto. *A quantum description of the beam splitter* (1995).
- [7] D. J. Brod et al. *Witnessing genuine multiphoton indistinguishability*. Physical Review Letters, 122 (2019).
- [8] A. Crespi et al. *Integrated multimode interferometers with arbitrary designs for photonic boson sampling*. Nature Photonics, 7, 545–549 (2013).
- [9] A. E. Moylett and P. S. Turner. *Quantum simulation of partially distinguishable boson sampling*. Physical Review A, 97 (2018).
- [10] J. P. Dowling. *Quantum optical metrology – the lowdown on high-n00n states*. Contemporary Physics, 49, 125–143 (2008).
- [11] V. Giovannetti et al. *Advances in quantum metrology*. Nature Photonics 5, 222 (2011) (2011).
- [12] J. C. Matthews et al. *Towards practical quantum metrology with photon counting*. npj Quantum Information, 2 (2016).
- [13] M. C. Tichy et al. *Zero-transmission law for multiport beam splitters*. Physical Review Letters, 104 (2010).

## BIBLIOGRAPHY

---

- [14] S. Aaronson and A. Arkhipov. *The computational complexity of linear optics*. In *Proceedings of the 43rd annual ACM symposium on Theory of computing - STOC '11*. ACM Press (2011).
- [15] M. A. Broome et al. *Photonic boson sampling in a tunable circuit*. *Science*, 339, 794–798 (2012).
- [16] J. B. Spring et al. *Boson sampling on a photonic chip*. *Science*, 339, 798–801 (2012).
- [17] M. Tillmann et al. *Experimental boson sampling*. *Nature Photonics*, 7, 540–544 (2013).
- [18] H.-S. Zhong et al. *Quantum computational advantage using photons*. *Science*, 370, 1460–1463 (2020).
- [19] R. Demkowicz-Dobrzański et al. *Quantum limits in optical interferometry*. In *Progress in Optics*, pages 345–435. Elsevier (2015).
- [20] K. J. Resch et al. *Time-reversal and super-resolving phase measurements*. *Physical Review Letters*, 98, 223601 (2007).
- [21] J. P. Olson et al. *Linear optical quantum metrology with single photons: Experimental errors, resource counting, and quantum cramer-rao bounds*. *Physical Review A*, 96, 013810 (2017).
- [22] A. Crespi. *Suppression laws for multiparticle interference in sylvester interferometers*. *Physical Review A*, 91 (2015).
- [23] N. Spagnolo et al. *Three-photon bosonic coalescence in an integrated tritter*. *Nature Communications*, 4 (2013).
- [24] A. Crespi et al. *Suppression law of quantum states in a 3d photonic fast fourier transform chip*. *Nature Communications*, 7 (2016).
- [25] N. Viggianiello et al. *Experimental generalized quantum suppression law in sylvester interferometers*. *New Journal of Physics*, 20, 033017 (2018).
- [26] T. Giordani et al. *Experimental quantification of four-photon indistinguishability*. *New Journal of Physics*, 22, 043001 (2020).
- [27] C. Antón et al. *Interfacing scalable photonic platforms: solid-state based multiphoton interference in a reconfigurable glass chip*. *Optica*, 6, 1471 (2019).
- [28] A. J. Menssen et al. *Distinguishability and many-particle interference*. *Physical Review Letters*, 118 (2017).
- [29] E. F. Galvão and D. J. Brod. *Quantum and classical bounds for two-state overlaps*. *Physical Review A*, 101, 062110 (2020).
- [30] H. E. Rose. *Linear Algebra*. Birkhäuser Basel (2002).

## BIBLIOGRAPHY

---

- [31] K. M. Davis et al. *Writing waveguides in glass with a femtosecond laser*. Optics Letters, 21, 1729 (1996).
- [32] T. Meany et al. *Engineering integrated photonics for heralded quantum gates*. Scientific Reports, 6 (2016).
- [33] S. Minardi and T. Pertsch. *Interferometric beam combination with discrete optics*. Optics Letters, 35, 3009 (2010).
- [34] R. Osellame et al., editors. *Femtosecond Laser Micromachining*. Springer Berlin Heidelberg (2012).
- [35] L. Keldysh. *Ionization in the field of a strong electromagnetic wave*. J. Exp. Theor. Phys, 20, 1307–1314 (1965).
- [36] C. B. Schaffer et al. *Laser-induced breakdown and damage in bulk transparent materials induced by tightly focused femtosecond laser pulses*. Measurement Science and Technology, 12, 1784–1794 (2001).
- [37] S. M. Eaton et al. *Heat accumulation effects in femtosecond laser-written waveguides with variable repetition rate*. Optics Express, 13, 4708 (2005).
- [38] C. Hnatovsky et al. *Fabrication of microchannels in glass using focused femtosecond laser radiation and selective chemical etching*. Applied Physics A, 84, 47–61 (2006).
- [39] E. N. Glezer et al. *Three-dimensional optical storage inside transparent materials*. Optics Letters, 21, 2023 (1996).
- [40] J. W. Chan et al. *Structural changes in fused silica after exposure to focused femtosecond laser pulses*. Optics Letters, 26, 1726 (2001).
- [41] Y. Shimotsuma et al. *Self-organized nanogratings in glass irradiated by ultra-short light pulses*. Physical Review Letters, 91 (2003).
- [42] S. Juodkazis et al. *Application of femtosecond laser pulses for microfabrication of transparent media*. Applied Surface Science, 197-198, 705–709 (2002).
- [43] T. F. Johnston. *Beam propagation ( $m^2$ ) measurement made as easy as it gets: the four-cuts method*. Applied Optics, 37, 4840 (1998).
- [44] G. Cerullo et al. *Femtosecond micromachining of symmetric waveguides at 15  $\mu\text{m}$  by astigmatic beam focusing*. Optics Letters, 27, 1938 (2002).
- [45] M. Ams et al. *Slit beam shaping method for femtosecond laser direct-write fabrication of symmetric waveguides in bulk glasses*. Optics Express, 13, 5676 (2005).
- [46] A. Arriola et al. *Low bend loss waveguides enable compact, efficient 3d photonic chips*. Optics Express, 21, 2978 (2013).

## BIBLIOGRAPHY

---

- [47] W.-J. Chen et al. *Broadband directional couplers fabricated in bulk glass with high repetition rate femtosecond laser pulses*. Optics Express, 16, 11470 (2008).
- [48] A. Crespi et al. *Measuring protein concentration with entangled photons*. Applied Physics Letters, 100, 233704 (2012).
- [49] O. Svelto. *Principles of Lasers*. Springer US (2010).
- [50] A. M. Streltsov and N. F. Borrelli. *Fabrication and analysis of a directional coupler written in glass by nanojoule femtosecond laser pulses*. Optics Letters, 26, 42 (2001).
- [51] I. Pitsios et al. *Geometrically-controlled polarisation processing in femtosecond-laser-written photonic circuits*. Scientific Reports, 7 (2017).
- [52] G. Corrielli et al. *Symmetric polarization-insensitive directional couplers fabricated by femtosecond laser writing*. Optics Express, 26, 15101 (2018).
- [53] L. Sansoni et al. *Polarization entangled state measurement on a chip*. Physical Review Letters, 105, 200503 (2010).
- [54] M. Gräfe et al. *On-chip generation of high-order single-photon  $w$ -states*. Nature Photonics, 8, 791–795 (2014).
- [55] J. Mower et al. *High-fidelity quantum state evolution in imperfect photonic integrated circuits*. Phys. Rev. A, 92, 032322 (2015).
- [56] J. Carolan et al. *Universal linear optics*. Science, 349, 711–716 (2015).
- [57] F. Flamini et al. *Thermally reconfigurable quantum photonic circuits at telecom wavelength by femtosecond laser micromachining*. Light: Science & Applications, 4, e354–e354 (2015).
- [58] I. V. Dyakonov et al. *Reconfigurable photonics on a glass chip*. Physical Review Applied, 10 (2018).
- [59] E. Polino et al. *Experimental multiphase estimation on a chip*. Optica, 6, 288 (2019).
- [60] F. Ceccarelli et al. *Thermal phase shifters for femtosecond laser written photonic integrated circuits*. Journal of Lightwave Technology, 37, 4275–4281 (2019).
- [61] D. Gloge. *Bending loss in multimode fibers with graded and ungraded core index*. Applied Optics, 11, 2506 (1972).
- [62] A. Yariv. *Coupled-mode theory for guided-wave optics*. IEEE Journal of Quantum Electronics, 9, 919–933 (1973).
- [63] R. W. F. Frederick W. Byron. *The Mathematics of Classical and Quantum Physics*. Dover Publications Inc. (1992).
- [64] A. Szameit et al. *Control of directional evanescent coupling in fs laser written waveguides*. Optics Express, 15, 1579 (2007).